Hopfield Neural Network method based Shunt Active Power Filter in PV integrated grid connected EV charging system

A DISSERTATION

SUBMITTED IN PARTIAL FULFILLMENT OF THE REQUIREMENTS
FOR THE AWARD OF THE DEGREE
OF
MASTER OF TECHNOLOGY
IN
CONTROL & INSTRUMENTATION

Submitted by

NAMAN KUMAR
(2K24/C&I/10)

Under the supervision of

Dr. ANKITA MATTA
Department of Electrical Engineering

DEPARTMENT OF ELECTRICAL ENGINEERING
DELHI TECHNOLOGICAL UNIVERSITY
(Formerly Delhi College of Engineering)
Bawana Road, Delhi 110042

MAY, 2026

M.TECH (Control & Instrumentation)

NAMAN KUMAR

2026

DEPARTMENT OF ELECTRICAL ENGINEERING
DELHI TECHNOLOGICAL UNIVERSITY
(Formerly Delhi College of Engineering)
Bawana Road, Delhi-110042

CANDIDATE'S DECLARATION

I, NAMAN KUMAR, Roll No. 2K24/C&I/10, student of M.Tech (Control & Instrumentation), hereby declare that the project Dissertation titled "Hopfield Neural Network method based Shunt Active Power Filter in PV integrated grid connected EV charging system" which is submitted by me to the Department of Electrical Engineering, Delhi Technological University, Delhi in partial fulfillment of the requirement for the award of degree of Master of Technology, is original and not copied from any source without proper citation. This work has not previously formed the basis for the award of any Degree, Diploma, Associateship, Fellowship or other similar title or recognition.

Place: Delhi

Date: 29/05/2026

Naman Kumar
(2K24/C&I/10)

DEPARTMENT OF ELECTRICAL ENGINEERING
DELHI TECHNOLOGICAL UNIVERSITY
(Formerly Delhi College of Engineering)
Bawana Road, Delhi-110042

CERTIFICATE

I hereby certify that the Project Dissertation titled "Hopfield Neural Network method based Shunt Active Power Filter in PV integrated grid connected EV charging system" which is submitted by NAMAN KUMAR, Roll No. 2K24/C&I/10, Department of Electrical Engineering, Delhi Technological University, Delhi in partial fulfillment of the requirement for the award of the degree of Master of Technology, is a record of the project work carried out by the student under my supervision. To the best of my knowledge this work has not been submitted in part or full for any Degree or Diploma to this University or elsewhere.

29/5/26.

Place: Delhi

Dr. Ankita Matta

Date: 29/5/26

SUPERVISOR

Assistant Professor
Department of Electrical Engineering
Delhi Technological University

DEPARTMENT OF ELECTRICAL ENGINEERING
DELHI TECHNOLOGICAL UNIVERSITY
(Formerly Delhi College of Engineering)
Bawana Road, Delhi-110042

ACKNOWLEDGEMENT

I express my sincere gratitude to **Dr. Ankita Matta** for guidance, support, and technical direction during the preparation of this project dissertation. I also thank the Department of Electrical Engineering, Delhi Technological University, for providing the academic environment required to study power quality, power-electronic converters, and renewable-energy integrated charging systems.

I am thankful to my teachers, classmates, and colleagues for their suggestions during the development of the simulation-based study. I also acknowledge the source papers and thesis documents cited in this report, which were used as technical references for SAPF design, Hopfield neural network control, PV-battery system configuration, and Lyapunov Hopfield current & voltage-reference control.

Place: Delhi

Date: 29/05/2026

Naman Kumar
(2K24/C&I/10)

ABSTRACT

This work compares two reference current estimation methods for a single-phase Shunt Active Power Filter (SAPF) applied to a photovoltaic (PV) integrated grid-connected Electric Vehicle (EV) charging system. Diode-rectifier EV chargers introduce harmonic currents at the point of common coupling (PCC); without compensation, source current THD readily exceeds the 5% limit prescribed by IEEE Std 519-2014.

The two methods examined are the Hopfield Neural Network (HNN) method and the Generalized Integrator (GI) method. In the HNN approach, load current is decomposed into in-phase and quadrature components whose estimation dynamics share a Lyapunov–Hopfield energy function, guaranteeing asymptotic stability. The GI uses a second-order resonant integrator tuned at 50 Hz to extract the fundamental component without phase lag; it is simpler to implement but its fixed resonant frequency reduces robustness under load transients.

The full system, a 110 V, 50 Hz single-phase grid, diode-rectifier EV load, PV array with MPPT-controlled boost converter, 154 V lead-acid battery with bidirectional buck–boost converter, and a VSC-based SAPF was modelled in MATLAB/Simulink. Both controllers were tested under steady-state operation, a step reduction in irradiance from 1000 W/m^2 to 500 W/m^2 at $t = 3.5$ s, and a load step. The HNN achieves a source current THD of 3.61% against 4.35% for the GI, a 17.01% relative reduction, with both values within the IEEE 519-2014 limit. The HNN also shows tighter DC-link voltage regulation and faster settling under transients. The power balance holds throughout the 5 s simulation for both controllers. These results indicate that the HNN is preferable where precise harmonic compensation is required; the GI remains a viable alternative under less demanding operating conditions.

Contents

List of Tables

List of Figures

List of Symbols and Abbreviations

Symbols

v_s, V_s	Instantaneous and rms grid supply voltage (V)
i_s	Source current (A)
i_L	Load current (A)
i_c	Compensating current injected by SAPF (A)
i_s^*	Reference source current (A)
i_L^*	Estimated fundamental load current (A)
i_{Lest}	Estimated amplitude of fundamental load current (A)
i_{dn}, i_{qn}	n^{th} harmonic d-axis and q-axis components (A)
ψ_{ka}	Hopfield energy / Lyapunov objective function
R_{an}	HNN weight matrix
S_{an}	HNN basis function vector
K	Positive gain constant of HNN
ω, ω_c	Grid angular frequency, GI resonant frequency (rad/s)
f_s	Switching frequency of VSC (Hz)
V_{dc}	DC link voltage (V)
V_{dc}^*, V_{dcref}	Reference DC link voltage (V)
C_{dc}	DC link capacitor (F)
L_f	Interfacing inductor of SAPF (H)
L_s	Source side inductance (H)
R_L, L_L	Resistance and inductance of nonlinear load
I_{loss}	Loss current component from DC link PI controller (A)
K_p, K_I	PI controller gains
e_{dc}	DC link voltage error
u_i	Unit in-phase template
V_t	Peak of supply voltage (V)
P_{Load}, Q_{Load}	Active and reactive power at load (W, VAR)
P_{grid}, Q_{grid}	Active and reactive power at source (W, VAR)
P_{VSC}, Q_{VSC}	Active and reactive power at VSC (W, VAR)
P_{PV}, V_{PV}, I_{PV}	PV array power, voltage and current
V_{batt}, I_{batt}	Battery terminal voltage and current
SOC	State of Charge of battery (%)
m	Modulation index
D	Duty cycle of DC-DC converter
a	Overloading factor
h_{band}	Hysteresis band of HCC (A)

Abbreviations

SAPF	Shunt Active Power Filter
VSC	Voltage Source Converter
EV	Electric Vehicle
PV	Photovoltaic
HNN	Hopfield Neural Network
GI	Generalized Integrator
SOGI	Second Order Generalized Integrator
SRFT	Synchronous Reference Frame Theory
PCC	Point of Common Coupling
MPPT	Maximum Power Point Tracking
THD	Total Harmonic Distortion
PLL	Phase Locked Loop
PWM	Pulse Width Modulation
IGBT	Insulated Gate Bipolar Transistor
HCC	Hysteresis Current Controller
G2V	Grid to Vehicle
V2G	Vehicle to Grid
BES	Battery Energy Storage
PI	Proportional Integral
LMS	Least Mean Square
LLMF	Leaky Least Mean Fourth
ADALINE	Adaptive Linear Neuron
RBF	Radial Basis Function
LPF	Low Pass Filter
BPF	Band Pass Filter
DSP	Digital Signal Processor
FPGA	Field Programmable Gate Array
RES	Renewable Energy Source
DC	Direct Current
AC	Alternating Current
RMS	Root Mean Square
P&O	Perturb and Observe
DSTATCOM	Distribution Static Compensator
UPQC	Unified Power Quality Conditioner
DVR	Dynamic Voltage Restorer
IEEE	Institute of Electrical and Electronics Engineers

CHAPTER 1

INTRODUCTION

1.1 General

Electricity, in today's world, is no longer a luxury but a basic need of life. The way it is produced, distributed and consumed has changed quite a lot in the last two decades. The growing interest in renewable energy sources like solar (PV) and wind energy has changed the structure of conventional power systems. At the same time, the transport sector is also moving towards electric mobility. The number of Electric Vehicles (EVs) on the road has been increasing year after year all over the world. Both of these changes, although individually very useful, have created new challenges for the operation of distribution networks. The most important of these challenges is the deterioration of *power quality*.

Power quality (PQ) refers to the property of the electrical supply by which all the equipment connected to it can operate in the normal manner without any malfunction [1,2]. Ideally, the voltage and current waveforms in a power system should be perfectly sinusoidal, balanced and at fixed frequency. In practice however, due to various reasons, these waveforms get distorted. The distortion is usually quantified using the Total Harmonic Distortion (THD), which measures how much of the waveform consists of harmonic components that are different from the fundamental.

Nonlinear loads are the main cause of harmonic distortion in modern distribution systems. A nonlinear load is one that draws a non-sinusoidal current even when the supply voltage is sinusoidal. Diode bridge rectifiers, switched mode power supplies, variable frequency drives and most importantly the EV chargers fall under this category. When such loads are connected at the Point of Common Coupling (PCC), the source current becomes highly distorted and contains many odd harmonics like the 3rd, 5th, 7th and so on. These harmonics cause many problems. They increase the losses in transformers and cables, cause overheating of motors, lead to malfunctioning of sensitive electronic equipment and may even trip the protection relays unnecessarily [3–5].

To control these harmonics, several techniques have been developed over the years. Passive filters were the first attempt and they consisted of tuned LC circuits that provided a low impedance path to specific harmonic frequencies [6–8]. While passive filters are simple and inexpensive, they have their own limitations. They are tuned at a fixed frequency, so they cannot adapt to changes in the load. They are also bulky and may resonate with the source impedance, sometimes making the problem worse. To overcome these issues, active power filters (APFs) were introduced. Among different types of APFs, the Shunt Active Power Filter (SAPF), which is connected in parallel with the load at PCC, has emerged as the most popular choice [9, 10]. It can dynamically adapt to changing load conditions and provide accurate harmonic compensation in real time.

A SAPF works on a very simple principle. It senses the load current, calculates the harmonic part of it, and then injects an equal and opposite current at the PCC so that the source side current becomes nearly sinusoidal. The hardware of a SAPF is essentially a Voltage Source Converter (VSC) with a DC link capacitor on one side and the AC system on the other side. The VSC is operated using suitable switching algorithms to produce the required compensating current. The performance of the SAPF mainly depends on two things: (i) the topology of the VSC and the design of its passive components, and (ii) the control algorithm used to generate the reference compensating current. Among these two, the control algorithm is the more critical one. Even with the best hardware, a poorly designed control algorithm can give very bad compensation results.

The integration of PV systems with the distribution network adds another layer of complexity to this problem. PV systems generate DC power that depends on the solar irradiance, which keeps changing during the day. This DC power has to be converted to AC of grid quality and synchronized with the grid before injection. The same VSC that is used as a SAPF can also be used to perform this grid interfacing function. This is a very attractive arrangement because it allows the same power electronics hardware to do two jobs at once: harmonic compensation and PV power injection [11, 12]. However, the control algorithm now has to be smart enough to handle both tasks simultaneously, while also dealing with the intermittency of solar irradiance.

When a battery energy storage system is also added to this arrangement, things become even more interesting. The battery, connected through a bidirectional DC-DC converter, can store the excess PV energy when it is sunny and release it back to the load when needed. This kind of system, sometimes called a PV-BES (Photovoltaic with Battery Energy Storage) system, is the natural choice for EV charging stations. In such a station, the EV charger acts as a nonlinear load, the PV array provides clean energy, the battery acts as a buffer and the SAPF maintains good power quality at the PCC. The control of this entire system, especially the SAPF part, is what the present work focuses on.

1.2 Motivation

The motivation for this work comes from a real-world observation. As more and more EVs are getting introduced in cities, charging stations are also being set up everywhere. Many of these stations are getting integrated with rooftop solar PV systems and battery banks to reduce the load on the grid. However, the chargers used in these stations are mostly nonlinear loads. A typical Level-1 or Level-2 EV charger has a diode bridge rectifier at the front end followed by a DC-DC converter [13, 14]. The current drawn by this rectifier has a peaky waveform with high harmonic content. When several such chargers operate at the same time, the harmonic problem at the PCC becomes severe.

The IEEE Standard 519-2014 [15] lays down strict limits on the allowable harmonic content of source currents in distribution systems. For systems below 1 kV, the standard prescribes that the THD of the source current should not exceed 5%. Many EV charging stations fail to meet this limit unless some form of harmonic compensation is provided. The SAPF is the most practical solution and a lot of work has been reported on its design and control [16–18].

In the literature, many different reference current estimation algorithms have been proposed for SAPF. These include the Synchronous Reference Frame Theory (SRFT), Instantaneous Reactive Power Theory (p-q theory), Second Order Generalized Integrator (SOGI), Least Mean Square (LMS) based algorithms, ADALINE based algorithms, and various advanced neural network based methods [19–22]. Each algorithm has its own merits and demerits. Some are fast but unstable. Others are stable but slow. Some require complex parameter tuning. There is no single algorithm that is best for all applications.

Among the more advanced algorithms, the Hopfield Neural Network (HNN) based control algorithm has received considerable attention in the recent past [23,24]. The HNN is a recurrent neural network in which the objective function used during training is simultaneously a valid Lyapunov function for the underlying dynamical system. This gives the HNN an important property: *guaranteed asymptotic stability* of the estimation dynamics. This is a major advantage over many other algorithms whose stability is either not proved or has to be checked case by case.

At the same time, the Generalized Integrator (GI) based method has been used widely in single-phase grid-connected systems for various purposes [25–27]. The GI is essentially a band-pass filter built around a second-order resonant integrator. It is computationally simple, requires very few tuning parameters, and gives good results in steady state conditions.

However, when one looks at the existing literature, a clear gap emerges. The HNN based algorithm has been mostly studied in the context of three-phase systems. Its performance for single-phase SAPF, especially in a unified PV-battery-EV charging environment, has not been investigated in detail. Similarly, the GI based algorithm has been used in single-phase PV integration but not specifically for SAPF control in EV charging systems with battery storage. There is also no direct comparison between these two algorithms under identical operating conditions. This comparison is important because the choice of algorithm has a direct impact on the achieved THD, the transient performance, the computational complexity and the stability guarantees.

The present work is motivated by this gap. The aim is to take the HNN algorithm and use it for single-phase current estimation in a unified PV-battery-EV charging system, take the GI algorithm and apply it to the same system, and then compare the two under steady state as well as dynamic conditions. The comparison includes the THD performance, transient response, DC link voltage regulation and power balance. The goal is to establish which algorithm is more suitable for the kind of system being studied here, and to provide a clear quantitative basis for that conclusion.

1.3 Background on the Problem

1.3.1 Power Quality Issues in EV-PV Integrated Systems

The integration of EVs and PV systems into the distribution network brings unique power quality challenges. These challenges differ from those of conventional industrial loads in some important ways. First, EV charging is a stochastic load, meaning that the number and duration of charging events vary throughout the day. Second, the EV charger is a power electronic device, which means it is inherently a nonlinear load. Third, the PV generation is intermittent and depends on weather conditions. Fourth, in a PV-EV integrated system, both generation and consumption happen at the distribution level, which is a departure from the traditional unidirectional power flow.

These factors together create a power quality environment that is much more dynamic than what was seen in traditional distribution systems. Voltage sags and swells, harmonic distortion, voltage flicker, frequency deviation, unbalance, and DC offset are some of the issues that may occur [5, 28, 29]. Among these, harmonic distortion is the most common and the most damaging in the short term, which is why harmonic compensation has received the most attention.

1.3.2 Role of SAPF in Power Quality Improvement

The SAPF is connected at the PCC and works in current control mode. It senses the load current i_L, estimates the fundamental component of this current, computes the difference (which is the harmonic content) and injects a compensating current i_c such that the source side current becomes $i_s = i_L - i_c \approx$ sinusoidal. The DC link of the SAPF is maintained at a reference voltage V_{dc}^* by a PI controller. The reference compensating current is realized by switching the VSC using a Hysteresis Current Controller (HCC) or a similar fast inner loop.

The H-bridge configuration of the VSC is the standard choice for single-phase SAPF. It consists of four IGBT switches with anti-parallel diodes, and a single DC link capacitor on the DC side [30]. The interfacing inductor L_f on the AC side limits the rate of change of compensating current and helps in smoothing the high frequency switching ripples.

1.3.3 HNN and GI Methods at a Glance

The HNN method, formulates the fundamental current estimation as an optimization problem. The objective function is the squared error between the actual load current and an estimated load current expressed as a sum of sinusoidal components. The weights of these components (d-axis and q-axis amplitudes) are updated by following the negative gradient of the objective function. Because the objective function is at the same time a Lyapunov function for the weight dynamics, asymptotic convergence is guaranteed. The fundamental amplitude is then computed from the d- and q-axis weights as $i_{Lest} = \sqrt{i_d^2 + i_q^2}$.

The GI method, uses a Second Order Generalized Integrator (SOGI) tuned at the grid fundamental frequency $\omega = 314$ rad/s. The SOGI takes the load current as input and produces two outputs: an in-phase fundamental component $i_{L\alpha}$, and a quadrature fundamental component $i_{L\beta}$. The fundamental amplitude is then $i_{Lest} = \sqrt{i_{L\alpha}^2 + i_{L\beta}^2}$. The reference current at source is generated by the product of this amplitude with a unit in-phase template $\sin(\omega t)$ obtained from a SOGI based PLL.

1.4 Problem Statement

The specific problem addressed in this dissertation can be stated as follows:

Consider a single-phase grid-connected EV charging system in which a nonlinear EV load is supplied by the grid. A PV array is connected to the DC link of the SAPF through an MPPT controlled boost converter, and a battery is connected to the same DC link through a bidirectional buck-boost converter. The SAPF is realized using *an H-bridge VSC. The objective is to determine which reference current estimation algorithm gives better performance: the Hopfield Neural Network (HNN) method or the Generalized Integrator (GI) based method. The performance is to be evaluated in terms of (a) source current THD, (b) compliance with IEEE 519-2014, (c) transient response under irradiance variation and load step, (d) DC link voltage regulation, and (e) power balance maintenance.*

1.5 Objectives of the Present Work

The main objectives of this dissertation are:

1. To develop a complete MATLAB/Simulink model of a single-phase PV-battery-grid connected EV charging system with SAPF.
2. To adapt the HNN based reference current estimation algorithm, originally developed for three-phase systems, to the single-phase case considered in this work.
3. To implement the GI based reference current estimation algorithm for the same single-phase system.
4. To design the various components of the SAPF, including the DC link voltage, DC link capacitance and interfacing inductor.
5. To simulate the system under steady state operation, sudden irradiance change and load step, with both controllers in turn.
6. To compare the performance of the two controllers quantitatively in terms of THD, transient response, DC link voltage regulation and power balance.
7. To draw conclusions regarding which controller is more suitable for the kind of system studied, and to suggest directions for future work.

1.6 Scope and Limitations

The scope of this dissertation is limited to simulation studies in MATLAB/Simulink. Hardware implementation and experimental verification are not part of this work.

The system considered is single-phase only; extension to three-phase systems is left for future work. The comparison is restricted to HNN and GI based methods. The battery is modelled using a simplified lead-acid model, and detailed electrochemical modelling is not considered. PV panel mismatch and partial shading effects are also not studied. The grid is assumed to be stiff (constant frequency and voltage), and weak grid scenarios are not investigated.

These limitations do not affect the validity of the comparison being presented. They simply define the boundary of the present study and indicate the directions in which the work can be extended in the future.

1.7 Organization of the Thesis

The remainder of this thesis is organized as follows.

Chapter 2 presents a detailed literature review covering the various aspects of the problem. It covers the basics of power quality, the design and control of SAPF, the various reference current estimation algorithms reported in the literature, the integration of PV systems and batteries into distribution networks, and the specific challenges of EV charging from a power quality perspective. The chapter ends with the identification of research gaps that motivated this work.

Chapter 3 describes the configuration of the single phase PV-Battery-Grid connection EV charging system. This chapter further describes the configuration of the SAPF including the voltage across DC link, DC link capacitance and interfacing inductor. This chapter describes the maximum power point tracking technique (MPPT) algorithm, the bidirectional converter of the battery, and all the sensor circuits.

Chapter 4 presents the complete mathematical formulation of the HNN based control algorithm. Starting from the Fourier series decomposition of the load current, it derives the objective function, the weight update equations, and the amplitude estimation expression. The Lyapunov stability of the algorithm is established & suitably adapted to single-phase systems.

Chapter 5 presents the GI based control algorithm. The transfer functions of the SOGI structure are derived. The selection of the resonant frequency and the gain K is discussed. The reference source current generation procedure using the SOGI outputs and the unit template is explained. The chapter also discusses the limitations of the GI method, particularly its sensitivity to frequency drift.

Chapter 6 presents the MATLAB/Simulink simulation results. The simulation setup, parameter selection and various test conditions are described. The time-domain waveforms, THD spectra, power balance results, battery charging/discharging behaviour, and estimated load current comparison are all presented in detail. The results of both controllers are compared and discussed.

Chapter 7 concludes the dissertation. The main findings are summarised, the contributions of this work are highlighted, and several directions for future research are suggested.

The dissertation ends with a list of references and an Appendix that contains the complete list of simulation parameters.

CHAPTER 2

LITERATURE REVIEW

2.1 General

This chapter presents a review of the existing literature relevant to the present work. The aim of this chapter is to give the reader a good understanding of where the research community currently stands on the various aspects of the problem being studied. It covers the basic concepts of power quality, the design and control of Shunt Active Power Filters (SAPF), the various reference current estimation algorithms reported in the literature, the integration of PV systems and batteries into distribution networks, and the specific challenges of EV charging from a power quality perspective. Towards the end of the chapter, the gaps in the existing work are identified, and these gaps form the motivation for the present study.

The literature on power quality and active filters is huge, with thousands of papers published every year. So this review is not meant to be exhaustive. Instead, it focuses on the works that are most relevant to the kind of system being studied here, namely a single-phase PV integrated grid-connected EV charging system with battery storage and a SAPF for harmonic compensation.

2.2 Power Quality Problems in Distribution Systems

2.2.1 Definition and Classification

The term *power quality* is generally used to describe the property of the electrical supply by which all the equipment connected to it can operate normally without any malfunction. The IEEE Standard 1159-2009 [29] gives a detailed definition and classifies power quality problems into several categories: voltage sag and swell, voltage flicker, harmonic distortion, voltage unbalance, transients, interruptions and frequency variations. Among these, harmonic distortion is the most common in modern distribution systems because of the widespread use of power electronic loads.

Singh, Chandra and Al-Haddad in their book [1] provide a comprehensive treatment of power quality problems and their mitigation techniques. They classify mitigation methods into three categories: passive filters, active filters and hybrid filters. Moreno-Munoz [2] discusses power quality issues in a distributed generation environment.

2.2.2 Harmonics and Their Effects

Harmonics are sinusoidal components of the current or voltage waveform whose frequencies are integer multiples of the fundamental frequency. Odd harmonics like the 3rd, 5th and 7th are the most common in single-phase systems with rectifier loads. The IEEE Working Group on Power System Harmonics [31] gave an early overview of harmonic issues in power systems. Wakileh [32] has provided a detailed treatment in his book “Power Systems Harmonics”.

Harmonic distortion is usually measured using the Total Harmonic Distortion (THD), which is the ratio of the rms value of all harmonic components to the rms value of the fundamental. For source current, the THD should be kept below 5% as per IEEE Standard 519-2014 [15]. Higher values of THD lead to many problems: extra losses in transformers, derating of cables, malfunction of sensitive electronic equipment, audible noise in motors and unnecessary tripping of protection relays [33,34].

2.3 Compensation Devices for Power Quality Improvement

2.3.1 Passive Filters

Passive filters were the first attempt at harmonic mitigation. They consist of tuned LC circuits that provide a low impedance path to specific harmonic frequencies. Beres et al. [6] have given a comprehensive review of passive power filters for three-phase grid-connected VSCs. Das [7] has discussed the potentialities and limitations of passive filters. Although simple and inexpensive, passive filters suffer from several drawbacks. They are tuned at a fixed frequency and cannot adapt to changes in the load. They are also bulky, especially for low harmonic orders. They may resonate with the source impedance, sometimes amplifying the problem they were meant to solve. LCL filters [35] are an improvement over simple LC filters but they too have similar issues.

2.3.2 Active Power Filters

To overcome the limitations of passive filters, Active Power Filters (APFs) were introduced. APFs are essentially power electronic converters that produce a controllable compensating current (or voltage) which cancels the harmonics in the source current (or voltage). They can dynamically adapt to changing load conditions. APFs are classified based on their topology and connection:

- **Shunt Active Power Filter (SAPF):** Connected in parallel with the load. Used mainly for current harmonic compensation. This is the topology studied in this thesis.
- **Series Active Power Filter:** Connected in series with the supply. Used for voltage harmonics and voltage sag compensation [36–38].
- **Unified Power Quality Conditioner (UPQC):** A combination of shunt and series filters. Provides comprehensive power quality improvement [39,40].

2.4 Reference Current Estimation Algorithms for SAPF

The reference current estimation algorithm is the heart of the SAPF. It is responsible for extracting the fundamental component of the load current so that the harmonic part can be computed and compensated. A wide variety of such algorithms have been proposed in the literature.

2.4.1 Neural Network Based Algorithms

Neural networks have been used extensively for SAPF control because of their ability to learn from data and adapt to changing conditions. Haykin's book [41] is the standard reference for neural networks. Lin and Lee [42] discuss neuro-fuzzy systems.

Hopfield Neural Network (HNN): The HNN is a recurrent neural network in which the objective function used for training is also a Lyapunov function for the underlying dynamical system. This property guarantees asymptotic stability. Cirrincione et al. [43, 44] used adaptive neural filtering for single-phase DG with SAPF capability.

2.4.2 Generalized Integrator and SOGI Based Methods

The Generalized Integrator (GI) and its second-order version (SOGI) have become very popular for single-phase grid-connected systems. Shah et al. [25] used GI based control for single-stage grid interfaced SECS. Shah and Singh [26] developed a fourth-order GI control scheme. Saxena, Singh and Rai [27, 45, 46] have done extensive work on enhanced third-order GI techniques.

The SOGI itself was developed primarily for grid synchronization. Xiao et al. [47] developed a frequency-fixed SOGI based PLL. Kulkarni and John [48] designed a fast response single-phase PLL with DC offset rejection. Zhang et al. [49] used mixed second and third order GI for DC offset elimination.

2.4.3 Functional Link Neural Networks

A more recent class of algorithms uses functional link neural networks, in which the input is expanded using a basis of orthogonal polynomials before being processed by a neural network. The popular ones include the Trigonometric Functional Link Neural Network (TFLNN), Legendre Functional Neural Network (LFNN) [50–53], Chebyshev Functional Expansion Neural Network [24], and spline based filters [54–56]. These methods avoid the need for PLL and Park-Clark transformations. Lagrange interpolation based variants [57–59] are also reported.

Sicuranza and Carini [60–63] have studied the BIBO stability conditions for adaptive FLANN filters. Kumar et al. [64–69] from Bhim Singh's group have proposed many variants of these algorithms.

2.5 Photovoltaic Integration with Distribution Networks

2.5.1 PV Modelling and MPPT

PV systems generate DC power that depends on solar irradiance and temperature. A standard single-diode equivalent circuit is used to model the PV array. The maximum power point of the array changes with operating conditions, and so a Maximum Power Point Tracking (MPPT) algorithm is needed to keep the array operating at its optimal point. Several MPPT algorithms are reported: Perturb & Observe [70, 71], Incremental Conductance [72, 73], fuzzy logic [74, 75], ANN based [76], and many others.

2.5.2 PV Grid Integration

Various aspects of PV integration with the grid have been studied. Karimi et al. [77] reviewed the issues and impacts of PV penetration in distribution networks. Liu et al. [78] developed droop control for PV with two-stage power conversion. Jain and Singh [79] proposed an adjustable DC link voltage based control for multifunctional grid interfaced solar PV. Mirhosseini et al. [80] addressed ride-through capability of PV plants under grid faults. Mastromauro et al. [11] discussed control issues in single-stage PV systems. Kjaer et al. [12] reviewed single-phase grid-connected inverters for PV modules.

Bhim Singh's group has done extensive work on PV integration with SAPF capability. The ILST control algorithm [81], the HTF based control [82], neural detection based control [83], recursive digital filter [84], MGI control [85], and many others have been developed.

2.6 Use of Battery in PV System

The use of battery energy storage with PV systems is essential to reduce the intermittency of solar generation. Rallabandi et al. [86] cover integration of battery energy storage with multi-MW PV systems. Karthikeyan and Gupta [87] propose varying phase angle control for bidirectional converters in PV-battery systems.

2.7 EV Charging and Power Quality

The rapid increase in EV adoption has brought EV-specific power quality issues to the forefront. The IEC 61851-1 [88], while not cited in the works above directly, governs EV conductive charging system requirements. Recent works specifically addressing EV-PV integrated power quality include Amir et al. [13] who use intelligent learning for transition control and protection in solar PV integrated EV charging stations. Nayak and Mohanty [14] address grid connected EV charging/discharging rate management.

2.8 Synchronization Techniques

Although not the main focus of the present work, the unit template generation for the SAPF requires a synchronization technique. The standard SRF-PLL [89] works well in stiff grids but struggles under distorted conditions. SOGI based PLLs [47,49,90–92] are more robust. Adaptive Notch Filter (ANF) based PLLs [93] have also been proposed. Moving Average Filter based PLLs [94], Cascaded Delayed Signal Cancellation PLLs [95], and DFT based synchronization [96] are other alternatives. Kalman filter based synchronization [97–99] can handle weak grid conditions. Quadrature signal generation based on Goertzel algorithm [100] is another approach.

Singh et al. [101] developed adaptive neuron detection based control with active filtering. Tsai-Fu Wu et al. [102] treat single-phase PV inverters with active power filtering capability. Chaudhary and Rizwan [103] developed a QNBP NN-based Icosϕ algorithm for PV systems integrated with LV/MV grid.

2.9 Research Gaps and Motivation for the Present Work

Based on the literature review presented above, the following research gaps are identified:

1. **HNN for single-phase SAPF in PV-EV environment:** The HNN based control algorithm developed by Chittora [23] has been studied mainly for three-phase systems. Its adaptation to single-phase SAPF in a unified PV-battery-EV charging environment has not been investigated in detail.

2. **Direct comparison of HNN and GI:** A direct head-to-head comparison of the HNN method and the GI based method, under identical operating conditions in a PV-EV-Battery integrated system, is missing in the literature. This kind of comparison is important for practitioners who have to choose between these two algorithms for actual implementations.

3. **Dynamic performance comparison:** Most comparative studies focus on steady state THD only. The comparison under dynamic conditions like sudden irradiance change and load steps has not been done systematically.

4. **Power balance validation:** The validation of the power balance identity $P_{grid} + P_{VSC} = P_{Load}$ in a combined PV-Battery-EV-SAPF system, under both steady state and dynamic conditions, has not been clearly demonstrated for HNN vs GI comparison.

5. **Lyapunov stability advantage:** While the Lyapunov stability of HNN is well established theoretically, its practical advantage in the PV-EV charging context (in terms of better transient response, settling time and DC link regulation) has not been quantified.

The present work addresses these gaps by undertaking a systematic simulation based comparison of HNN and GI methods for SAPF control in a single-phase PV-Battery-grid-connected EV charging system. The detailed objectives and scope of this work were stated in Chapter 1. The next chapter describes the system configuration and the design of the various components in detail.

2.10 Summary

This chapter has presented a review of the literature on power quality, SAPF design and control, various reference current estimation algorithms, PV integration, battery storage, EV charging power quality and related synchronization techniques. The huge volume of work in this area was summarized under several thematic headings. The chapter ended with the identification of five specific research gaps that motivate the present study.

The next chapter describes the system configuration of the PV-Battery-grid-connected EV charging system with SAPF, adopting the PV-BES configuration from Arora's thesis (Section 3.1.3), and provides the detailed design calculations for the various components.

CHAPTER 3

SYSTEM CONFIGURATION AND DESIGN

3.1 General

This chapter describes the system configuration of the single-phase PV-Battery integrated grid-connected EV charging system with Shunt Active Power Filter (SAPF) that has been studied in this dissertation. The chapter also describes the PV array model, the MPPT algorithm, the bidirectional buck-boost converter for the battery, and the various sensor and gate drive arrangements.

The objective of this chapter is to give the reader a complete picture of the hardware setup as captured in the simulation model. Once this setup is clearly understood, the next two chapters describe the two control algorithms (HNN and GI) that are applied to this system, and Chapter 6 presents the simulation results.

3.2 Overall System Topology

The complete topology of the proposed system is shown in Fig. 3.1. It consists of the following main subsystems:

1. Single-phase AC grid with source impedance.
2. Nonlinear EV charging load.
3. Shunt Active Power Filter (SAPF) at PCC.
4. PV array with MPPT controlled boost converter connected at the DC link.
5. Lead-acid battery with bidirectional buck-boost converter connected at the same DC link.

6. Control system that includes the reference current estimation algorithm (HNN or GI), DC link voltage PI controller, and hysteresis current controller.

The single-phase sinusoidal AC grid supplies a voltage of $V_s = 110$ V rms at 50 Hz. The nonlinear load is realised by a single-phase diode bridge rectifier feeding a series R-L load. The resistance R_L varies from 20 to 120 Ω to emulate different EV charging states and load step transients. The inductance $L_L = 80$ mH provides some smoothing on the DC side of the rectifier.

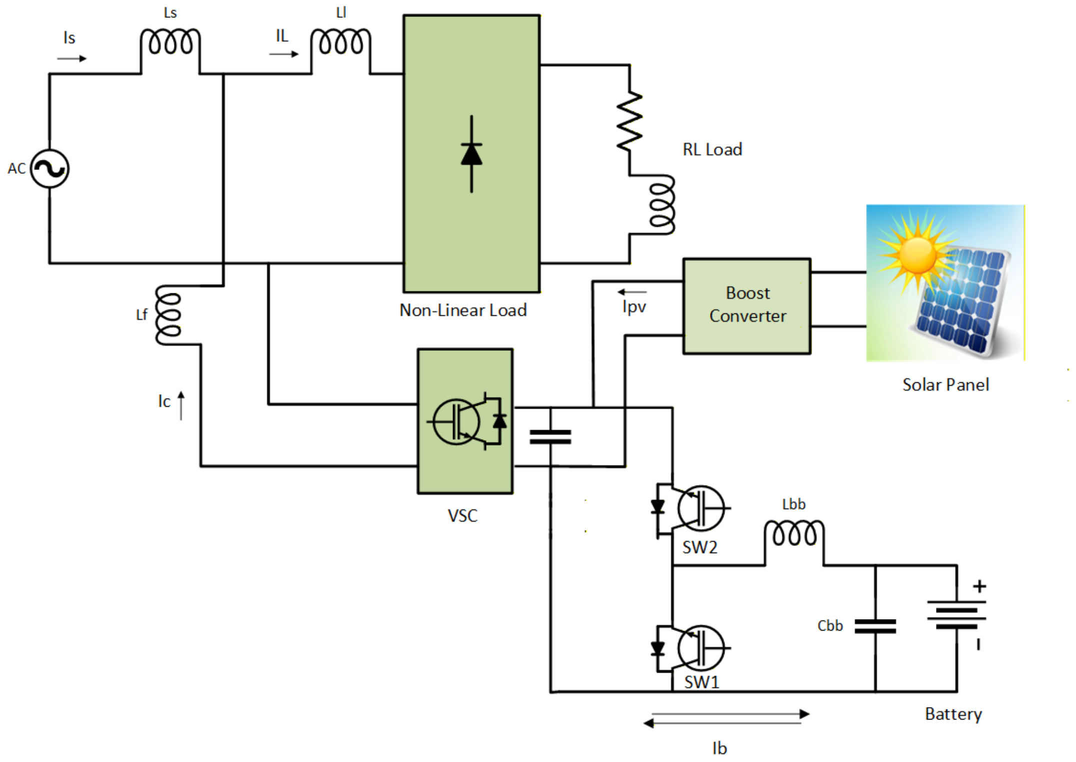

Figure 3.1: Topology of the proposed PV-Battery-grid-connected EV charging system with SAPF.

The SAPF is connected in parallel with the nonlinear load at the PCC through an interfacing inductor L_f. It consists of an H-bridge VSC formed by four IGBT switches with anti-parallel diodes, and a DC link capacitor C_{dc}. The DC link is shared between the SAPF, the PV boost converter and the battery bidirectional converter. This sharing allows the same VSC to perform multiple functions: harmonic compensation, PV power injection into the grid, and management of the battery charge/discharge.

The relation between the various currents at the PCC is given by Kirchhoff's current law:

$$i_s = i_L + i_c \tag{3.1}$$

where i_s is the source (grid) current, i_L is the nonlinear load current, and i_c is the compensating current injected by the SAPF. When the SAPF operates correctly, the compensating current cancels the harmonic content of the load current, making the source current i_s nearly sinusoidal and in phase with the supply voltage v_s.

3.3 Configuration of PV-BES System

The single-phase PV-Battery Energy Storage (PV-BES) system configuration, with appropriate adaptations for the present work. The block diagram of this PV-BES system is shown in Fig. 3.1. The key features of the configuration are described below.

3.3.1 PV Array and Boost Converter

The PV array is connected to the DC link through a DC-DC boost converter. The boost converter is operated under the control of a Maximum Power Point Tracking (MPPT) algorithm. The MPPT regulates the duty cycle of the boost converter so that the PV array always operates at its maximum power point under any irradiance and temperature condition. The Perturb and Observe (P&O) algorithm is used in this work because of its simplicity and proven reliability.

3.3.2 Battery and Bidirectional Converter

The battery is connected to the same DC link through a bidirectional buck-boost converter. The battery is a 154 V lead-acid battery with a nominal capacity of 20 Ah and an initial State of Charge (SOC) of 90%. The bidirectional converter has two switches:

- Switch SW1 (boost mode): When the battery is supplying power to the DC link (discharging mode), SW1 operates in PWM and SW2 is off.

- Switch SW2 (buck mode): When the battery is being charged from the DC link (charging mode), SW2 operates in PWM and SW1 is off.

This dual mode operation allows the battery to absorb the excess PV energy when the solar irradiance is high and to release stored energy when the PV is insufficient to meet the load demand. The bidirectional converter inductor L_{bb} and capacitor C_{bb} are designed to limit current and voltage ripples respectively.

3.4 Design of SAPF Components for Single-Phase System

This section presents the design calculations for the SAPF components, The procedure is specifically for single-phase systems.

3.4.1 DC Link Voltage V_{dc}

For proper operation of the SAPF, the DC link voltage must be greater than the peak of the supply voltage. This is needed so that the VSC can inject sufficient compensating current at all instants in the AC cycle. The minimum DC link voltage is computed as

$$V_{dc,min} = \sqrt{2}\,V_{rms} = \sqrt{2} \times 110 = 155.56 \text{ V} \tag{3.2}$$

An adequate margin above this minimum is provided to account for transients, losses and the need to support the boost converter operation. The chosen DC link voltage is

$$V_{dc} = V_{dcref} = 200 \text{ V} \tag{3.3}$$

This value provides a margin of about 28.6% above the calculated minimum.

3.4.2 DC Link Capacitance C_{dc}

The capacitor located on DC link is sized according to the principle of energy balance during transients. Sudden variation in load, the capacitor must be able to absorb or supply the transient energy without allowing V_{dc} to deviate too much from its reference value. The energy balance condition is

$$\frac{1}{2}C_{dc}\left(V_{dc}^2 - V_{dc1}^2\right) = K_1 V_{rms}\, a\, I\, t \tag{3.4}$$

Rearranging,

$$C_{dc} = \frac{2K_1 V_{rms}\, a\, I\, t}{V_{dc}^2 - V_{dc1}^2} \tag{3.5}$$

Substituting the values $K_1 = 0.5$, $V_{rms} = 110$ V, $I_{ph} = 20$ A, $t = 0.02$ s, $V_{dc} = 200$ V, $V_{dc1} = 155.56$ V, $a = 1.2$:

$$C_{dc} = \frac{2 \times 0.5 \times 110 \times 1.2 \times 20 \times 0.02}{200^2 - 155.56^2} = 3341\ \mu\text{F} \tag{3.6}$$

A standard commercially available value is selected:

$$C_{dc} = 3000\ \mu\text{F} \tag{3.7}$$

This is slightly lower than the calculated value but still acceptable considering the conservative overloading factor used.

3.4.3 Interfacing Inductor L_f

The interfacing inductor is used to limit the high frequency ripple in the compensating current injected by the SAPF. Its value depends on the modulation index m, the DC link voltage V_{dc}, the switching frequency f_s, the allowable current ripple I_{crpp} and the overloading factor a:

$$L_f = \frac{m\, V_{dc}}{4\, a\, f_s\, I_{crpp}} \tag{3.8}$$

Substituting $m = 1$, $V_{dc} = 200$ V, $a = 1.2$, $f_s = 10$ kHz, $I_{crpp} = 1.5$ A:

$$L_f = \frac{1 \times 200}{4 \times 1.2 \times 10 \times 10^3 \times 1.5} = 2.77\ \text{mH} \approx 3\ \text{mH} \tag{3.9}$$

The selected value is

$$L_f = 3\ \text{mH} \tag{3.10}$$

3.4.4 IGBT Module Rating

The IGBT switches must be rated for the maximum DC link voltage and the peak compensating current. With $V_{dc} = 200$ V and a peak compensating current of about 20 A, the IGBTs need a voltage rating of at least 400 V (allowing for 2x margin) and a current rating of at least 30 A. Such IGBT modules are commercially available from manufacturers like Infineon, IXYS and Semikron, and their use does not pose any practical difficulty.

3.5 PV Array Design

The PV array used in this simulation is based on the Kyocera Solar KD250GX-LFB2 panel. The panel specifications are summarised in Table 3.1.

Table 3.1: Specifications of the PV Panel (Kyocera Solar KD250GX-LFB2)

Parameter	**Value**
Maximum power P_{mp}	250.022 W
Open circuit voltage V_{oc}	36.9 V
Short circuit current I_{sc}	9.09 A
Maximum power voltage V_{mp}	29.8 V
Maximum power current I_{mp}	8.39 A
Series connected modules per string	3
Cells per module	60
Parallel strings	1
Temperature coefficient of voltage	-0.32 %/°C
Temperature coefficient of current	$+0.06$ %/°C
Sampling time	5 μs

With 3 panels in series, the array provides a maximum voltage of about $3 \times 29.8 = 89.4$ V and a maximum current of about 8.39 A under standard test conditions (1000 W/m^2 irradiance, 25°C). The total array power is approximately 750 W.

3.5.1 Boost Converter Design

The boost converter steps up the PV array voltage to the DC link voltage of 200 V. The duty cycle D in continuous conduction mode is given by:

$$D = 1 - \frac{V_{in}}{V_{out}} = 1 - \frac{89.4}{200} \approx 0.55 \tag{3.11}$$

The boost inductor L_b is chosen to limit the current ripple to about 20% of the average inductor current:

$$L_b = \frac{D \times V_{mp}}{\Delta I_{PV} \times f_{sw}} = \frac{0.55 \times 89.4}{0.81 \times 10 \times 10^3} \approx 5 \text{ mH} \tag{3.12}$$

A practical value $L_b = 5$ mH is selected. The boost capacitor C_b is selected to limit output voltage ripple:

$$C_b = \frac{D \times I_{out}}{\Delta V_{out} \times f_{sw}} \approx 150 \ \mu\text{F} \tag{3.13}$$

3.6 Battery and Bidirectional Buck-Boost Converter

The battery used in the simulation is a 154 V lead-acid battery with a nominal capacity of 20 Ah and an initial State of Charge of 90%. The battery is modelled using the standard Simscape Electrical battery block with the response time set to 0.1 s.

3.6.1 Bidirectional Buck-Boost Converter Design

In buck mode (battery charging), the duty cycle is:

$$D_{buck} = \frac{V_b}{V_{dc}} = \frac{154}{200} = 0.77 \tag{3.14}$$

The bidirectional converter inductor L_{bb} is sized to limit current ripple:

$$L_{bb} = \frac{D(V_{dc} - V_b)}{\Delta I_L \times f_{sw}} = \frac{0.77 \times (200 - 154)}{5 \times 10^3 \times 0.1 \times 7} \approx 1 \text{ mH} \tag{3.15}$$

A practical value $L_{bb} = 2$ mH is selected to provide a more conservative current ripple. The bidirectional converter capacitor $C_{bb} = 470\ \mu$F is selected for adequate output filtering.

3.6.2 Control of Bidirectional Converter

The bidirectional converter is controlled by a simple power balance logic. The net PV power available at the DC link is computed and compared with the load demand. If PV power exceeds load demand, the converter operates in buck mode to charge the battery. If PV power is less than load demand, the converter operates in boost mode to supplement the deficit. A hysteresis band around the threshold prevents rapid mode switching due to small fluctuations.

The SOC is monitored continuously. Discharging is inhibited if SOC falls below 20% to prevent deep discharge. Charging is inhibited if SOC exceeds 95% to prevent overcharging. These limits are based on standard practices for lead-acid batteries.

3.7 Reference Current Generation and Hysteresis Current Controller

This section describes the part of the control system that is common to both the HNN and GI algorithms. The specific algorithms are described in Chapters 4 and 5 respectively.

3.7.1 DC Link Voltage PI Controller

The DC link voltage is regulated by an outer PI controller. The error between the reference and the actual DC link voltage is given by

$$e_{dc}(k) = V_{dc}^*(k) - V_{dc}(k) = 200 - V_{dc}(k) \tag{3.16}$$

The PI controller output, which represents the loss current component I_{loss}, is updated as

$$I_{loss}(k) = I_{loss}(k-1) + K_p\{e_{dc}(k) - e_{dc}(k-1)\} + K_I\, e_{dc}(k) \tag{3.17}$$

The PI gains are $K_p = 0.1$ and $K_I = 1.0$. An anti-windup limit is applied to keep I_{loss} within $[-5, +5]$ A so that it does not grow unbounded during severe transients.

3.7.2 Reference Source Current Generation

The reference source current is generated as

$$i_s^* = (i_{Lest} + I_{loss}) \sin(\omega t) \tag{3.18}$$

Here, i_{Lest} is the estimated fundamental load current amplitude (from HNN or GI), I_{loss} accounts for the losses, and $\sin(\omega t)$ is the unit in-phase template synchronized with the grid voltage. The unit template is generated by a SOGI based PLL applied to the supply voltage v_s.

3.7.3 Hysteresis Current Controller

The HCC compares the actual source current i_s (or equivalently, the compensating current i_c) with the reference value. When the actual current goes below the reference minus the hysteresis band, the upper pair of IGBTs is switched ON. When it goes above the reference plus the hysteresis band, the lower pair is switched ON. The hysteresis band is set to $h_{band} = \pm 0.5$ A.

This simple HCC implementation gives variable switching frequency (the frequency depends on the operating point), with an average frequency of about 10 kHz under nominal conditions. While more sophisticated current control schemes (e.g. SVPWM, adaptive HCC) could give constant switching frequency, the simple HCC is adequate for the comparison study being undertaken here, and it keeps the simulation focused on the reference current estimation algorithms which are the main subject of comparison.

3.8 Complete System Parameter Summary

Table 3.2 provides a complete summary of all the simulation parameters used in this work. These values follow the design procedure described above and are consistent with the values used in Appendix III of Arora's thesis for the battery interfaced PV integrated grid connected system.

Table 3.2: Complete Simulation Parameters of the Proposed System

Parameter	**Value**
Grid voltage V_s	110 V rms, 50 Hz
Source impedance L_s	0.1 mH
Interfacing inductor L_f	3 mH
DC link capacitor C_{dc}	3000 μF
DC link reference voltage V_{dc}^*	200 V
Nonlinear load R_L	20–120 Ω
Nonlinear load L_L	80 mH
Battery type	Lead-acid, 154 V, 20 Ah
Initial SOC	90%
Battery response time	0.1 s
VSC topology	H-bridge (4 IGBTs)
IGBT switching frequency f_s	10 kHz
PV array	3 × Kyocera KD250GX-LFB2 (750 W total)
Boost inductor L_b	5 mH
Boost capacitor C_b	150 μF
Bidirectional converter inductor L_{bb}	2 mH
Bidirectional converter capacitor C_{bb}	470 μF
HCC hysteresis band	$\pm$0.5 A
DC link PI controller gains	$K_p = 0.1$, $K_I = 1.0$
HNN gain constant K	10
GI gain K	$\sqrt{2} \approx 1.414$
SOGI resonant frequency ω	314 rad/s
Simulation time step	50 μs
Total simulation time	5 s

3.9 Summary

This chapter has described the system configuration of the single-phase PV-Battery-grid-connected EV charging system with SAPF. The appropriate adaptations for the single-phase case. The single-phase SAPF component design procedure of Section 3.2.1 of the same thesis was followed to size the DC link voltage (200 V), DC link capacitor (3000 μF) and interfacing inductor (3 mH). The PV array (3×Kyocera KD250GX-LFB2, total 750 W), MPPT controlled boost converter, lead-acid battery (154 V, 20 Ah), bidirectional buck-boost converter, and the common control elements (DC link PI controller, reference current generation, HCC) were all described in detail. The complete simulation parameter set was tabulated in Table 3.2.

The next chapter presents the mathematical formulation of the HNN based reference current estimation algorithm, which is one of the two algorithms being compared in this work.

CHAPTER 4

HOPFIELD NEURAL NETWORK BASED CONTROL ALGORITHM

4.1 General

This chapter presents the complete mathematical formulation of the Hopfield Neural Network (HNN) based reference current estimation algorithm. The adaptation to the single-phase system is straightforward and is described in detail in this chapter.

The chapter begins with an overview of the Hopfield Neural Network architecture and its key property of having an energy function that is also a Lyapunov function. The Fourier series representation of the nonlinear load current is then derived, and used to define the objective function for the HNN. The matrix formulation that simplifies the analysis is introduced. The energy minimization condition is applied and the weight update equations are derived. The Lyapunov stability of the algorithm is established formally. Finally, the implementation of the HNN in MATLAB/Simulink is described.

4.2 Hopfield Neural Network Architecture

The Hopfield Neural Network (HNN) is a recurrent neural network introduced by John Hopfield in 1982. Unlike feedforward neural networks, the HNN has feedback connections between neurons. The output of each neuron is fed back to all other neurons in the network through weighted connections, but importantly, there is no self-feedback. The outputs are updated iteratively according to the network dynamics, until convergence is achieved.

The most important property of the HNN, which makes it attractive for many applications, is that it has an *energy function* that decreases monotonically along the network trajectories. This energy function is also a valid Lyapunov function for the underlying dynamical system. The existence of a Lyapunov function guarantees that the network will converge to a stable equilibrium for any initial conditions, which is a very strong property indeed.

For the SAPF application, the HNN is configured as a network of $2n$ neurons. Here, n is the number of harmonic frequencies to be considered. For each frequency, two neurons are needed: one for the in-phase (α) component and one for the quadrature (β) component. This is a multiple-loop feedback system with in-phase and quadrature extraction blocks at the fundamental frequency and harmonic frequencies. The HNN can be tuned at any specific frequency to extract harmonics from a non-linear signal having multiple frequency components.

In the present work, the focus is on the estimation of the fundamental component only. Higher order harmonics need not be estimated separately because they are computed indirectly as the difference between the load current and the estimated fundamental.

The block diagram of the HNN algorithm as adapted for single-phase systems is shown in Fig. 4.1.

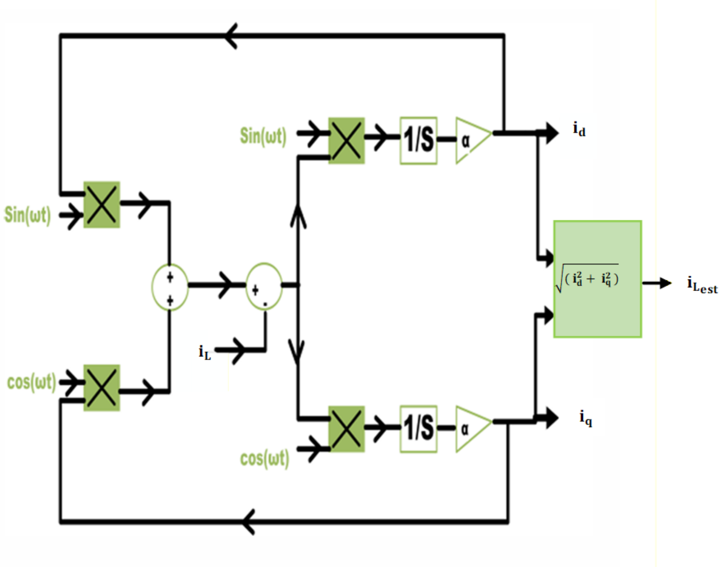

Figure 4.1: Block diagram of the Hopfield Neural Network based reference current estimation algorithm.

4.3 Fourier Decomposition of Load Current

The nonlinear load current $i_L(t)$ drawn by the EV charger contains harmonics in addition to the fundamental. Using Fourier series, the load current can be expressed as

$$i_L(t) = \sum_{m=1}^{N} I_m \sin(m\omega t + \theta_m) \tag{4.1}$$

where I_m is the peak magnitude of the m^{th} harmonic component and θ_m is its phase angle. The fundamental angular frequency is $\omega = 2\pi f$ where $f = 50$ Hz in this work, so $\omega = 314$ rad/s.

Using the trigonometric identity $\sin(m\omega t+\theta_m) = \sin(m\omega t)\cos(\theta_m)+\cos(m\omega t)\sin(\theta_m)$, the above expression can be rewritten as

$$i_L(t) = \sum_{m=1}^{N} [\alpha_m \sin(m\omega t) + \beta_m \cos(m\omega t)] \tag{4.2}$$

where the in-phase and quadrature components are defined as $\alpha_m = I_m \cos\theta_m$ and $\beta_m = I_m \sin\theta_m$.

This decomposition is the basis of the HNN approach: instead of estimating the magnitudes and phase angles $\{I_m, \theta_m\}$ directly, we estimate the in-phase and quadrature components $\{\alpha_m, \beta_m\}$. From these, the peak magnitude I_m and phase θ_m can be recovered easily if needed:

$$I_m = \sqrt{\alpha_m^2 + \beta_m^2}, \quad \theta_m = \tan^{-1}\frac{\beta_m}{\alpha_m} \tag{4.3}$$

4.4 Objective Function for HNN

Now we set up the HNN as an estimator. Let $i_L^*(t)$ denote the estimated load current. We will use the same Fourier representation for the estimate:

$$i_L^*(t) = \sum_{n=1}^{N} [i_{dn} \sin(n\omega t) + i_{qn} \cos(n\omega t)] \tag{4.4}$$

where i_{dn} and i_{qn} are the estimated d-axis (in-phase) and q-axis (quadrature) weights respectively. These weights are what the HNN will update iteratively.

The objective function ψ_{ka} is defined as the squared error between the estimated and actual load currents:

$$\psi_{ka} = 0.5\,[i_L^*(t) - i_L(t)]^2 \tag{4.5}$$

Equivalently, summing over the components:

$$\psi_{ka} = 0.5\left[\sum_{n=1}^{N}(i_{dn}\sin(n\omega t) + i_{qn}\cos(n\omega t)) - i_L\right]^2 \tag{4.6}$$

This ψ_{ka} is the Hopfield energy function. It is non-negative (because it is a square) and equals zero only when the estimation is perfect, i.e. $i_L^* = i_L$. Minimizing this energy function therefore amounts to estimating i_L as accurately as possible using the chosen basis functions.

4.5 Matrix Formulation

The expressions above can be written compactly using matrix notation. Define the weight matrix R_{an} and the basis function matrix S_{an} as

$$R_{an} = \begin{bmatrix} i_{d1} & i_{q1} & i_{d2} & i_{q2} & \cdots & i_{dN} & i_{qN} \end{bmatrix} \tag{4.7}$$

$$S_{an} = \begin{bmatrix} \sin(\omega t) \\ \cos(\omega t) \\ \sin(2\omega t) \\ \cos(2\omega t) \\ \vdots \\ \sin(N\omega t) \\ \cos(N\omega t) \end{bmatrix} \tag{4.8}$$

Note that R_{an} is a row vector containing the weights, and S_{an} is a column vector containing the time-varying basis functions. With these definitions, the estimated load current can be written as

$$i_L^*(t) = R_{an}\,S_{an} \tag{4.9}$$

The objective function takes the compact form (Eq. 4.21 of Chittora's thesis):

$$\psi_{ka} = 0.5\,[R_{an}\,S_{an} - i_L]^2 \tag{4.10}$$

This is a quadratic function of the weights R_{an}. Quadratic functions have a unique global minimum, so the HNN is guaranteed to find that minimum regardless of the initial condition. This is an important point: the convexity of the objective function is what gives the HNN its global convergence property.

4.6 Energy Minimization and Weight Update Equations

The HNN seeks to minimize the objective function. The minimization is achieved by applying the gradient descent principle: at each instant of time, the weights are updated in the direction of the negative gradient of ψ_{ka}.

Mathematically, the minimization condition is

$$\frac{d\psi_{ka}}{dt} = 0 \tag{4.11}$$

The gradient descent update is:

$$\frac{\partial R_{an}}{\partial t} = -K\frac{\partial \psi_{ka}}{\partial R_{an}} \tag{4.12}$$

where K is a positive gain constant. The sign is negative because we want to move *against* the gradient (downhill on the energy surface).

Expanding R_{an} into its components:

$$\frac{\partial}{\partial t}\begin{bmatrix} i_{d1} & i_{q1} & \cdots & i_{dN} & i_{qN} \end{bmatrix} = -K\frac{\partial \psi_{ka}}{\partial R_{an}} \tag{4.13}$$

Separating into d-axis and q-axis components:

$$\sum_{n=1}^{N}\frac{\partial i_{dn}}{\partial t} = -K\sum_{n=1}^{N}\frac{\partial \psi_{ka}}{\partial i_{dn}} \tag{4.14}$$

$$\sum_{n=1}^{N} \frac{\partial i_{qn}}{\partial t} = -K \sum_{n=1}^{N} \frac{\partial \psi_{ka}}{\partial i_{qn}} \tag{4.15}$$

Now we compute the partial derivatives. Differentiating Eq. 4.6 with respect to i_{dn}:

$$\frac{\partial \psi_{ka}}{\partial i_{dn}} = \left[\sum_{n=1}^{N} (i_{dn} \sin(n\omega t) + i_{qn} \cos(n\omega t)) - i_L \right] \sin(n\omega t) \tag{4.16}$$

Similarly, differentiating with respect to i_{qn}:

$$\frac{\partial \psi_{ka}}{\partial i_{qn}} = \left[\sum_{n=1}^{N} (i_{dn} \sin(n\omega t) + i_{qn} \cos(n\omega t)) - i_L \right] \cos(n\omega t) \tag{4.17}$$

Substituting these partial derivatives into Eqs. 4.14 and 4.15:

$$\frac{\partial i_{dn}}{\partial t} = -K \left[\sum_{n=1}^{N} (i_{dn} \sin(n\omega t) + i_{qn} \cos(n\omega t)) - i_L \right] \sin(n\omega t) \tag{4.18}$$

$$\frac{\partial i_{qn}}{\partial t} = -K \left[\sum_{n=1}^{N} (i_{dn} \sin(n\omega t) + i_{qn} \cos(n\omega t)) - i_L \right] \cos(n\omega t) \tag{4.19}$$

Integrating both sides with respect to time, the final update equations are obtained:

$$\boxed{i_{dn} = -K \int \left\{ \left[\sum_{n=1}^{N} (i_{dn} \sin(n\omega t) + i_{qn} \cos(n\omega t)) - i_L \right] \sin(n\omega t) \right\} dt} \tag{4.20}$$

$$\boxed{i_{qn} = -K \int \left\{ \left[\sum_{n=1}^{N} (i_{dn} \sin(n\omega t) + i_{qn} \cos(n\omega t)) - i_L \right] \cos(n\omega t) \right\} dt} \tag{4.21}$$

These two coupled integral equations are the core of the HNN algorithm. They are implemented in MATLAB/Simulink using integrator blocks, multipliers and sine/cosine generators.

4.7 Fundamental Amplitude Estimation

For the SAPF application, we are interested only in the fundamental component, i.e. $n = 1$. With $n = 1$, the update equations become

$$i_d = -K \int \{[(i_d \sin(\omega t) + i_q \cos(\omega t)) - i_L] \sin(\omega t)\}\, dt \tag{4.22}$$

$$i_q = -K \int \{[(i_d \sin(\omega t) + i_q \cos(\omega t)) - i_L] \cos(\omega t)\}\, dt \tag{4.23}$$

The estimated amplitude of the fundamental load current is then obtained by combining the d-axis and q-axis components:

$$\boxed{i_{Lest} = \sqrt{i_d^2 + i_q^2}} \tag{4.24}$$

This i_{Lest} is the key output of the HNN algorithm. It represents the peak amplitude of the fundamental component of the load current. This value is then used in the reference source current generation as described in Chapter 3.

4.8 Lyapunov Stability Analysis

This is one of the most important properties of the HNN algorithm: the dynamics described by Eqs. 4.20 and 4.21 are guaranteed to be asymptotically stable. The proof uses Lyapunov's direct method.

Theorem (Asymptotic stability of HNN): Consider the objective function ψ_{ka} defined in Eq. 4.10. Under the weight update rule Eq. 4.12, the function ψ_{ka} is a valid Lyapunov function and the system is asymptotically stable.

Proof: For ψ_{ka} to be a Lyapunov function, the following three conditions must be satisfied:

(i) *Positive definiteness:* From Eq. 4.10, $\psi_{ka} \geq 0$ for all R_{an}, and $\psi_{ka} = 0$ only when $R_{an}S_{an} = i_L$. So ψ_{ka} is positive definite at the unique minimum point.

(ii) *Radial unboundedness:* As $\|R_{an}\| \to \infty$, $\psi_{ka} \to \infty$. This is obvious from the quadratic form of ψ_{ka}.

(iii) *Negative definiteness of the time derivative:* Computing $d\psi_{ka}/dt$ using the chain rule:

$$\frac{d\psi_{ka}}{dt} = \frac{\partial \psi_{ka}}{\partial R_{an}} \cdot \frac{dR_{an}}{dt} \tag{4.25}$$

Substituting the gradient descent update rule (Eq. 4.12):

$$\frac{d\psi_{ka}}{dt} = \frac{\partial \psi_{ka}}{\partial R_{an}} \cdot \left(-K\frac{\partial \psi_{ka}}{\partial R_{an}}\right) = -K\left\|\frac{\partial \psi_{ka}}{\partial R_{an}}\right\|^2 \tag{4.26}$$

Since $K > 0$ and the square norm is non-negative,

$$\frac{d\psi_{ka}}{dt} \leq 0 \tag{4.27}$$

The equality holds only at the equilibrium point where the gradient is zero, which corresponds to $R_{an}S_{an} = i_L$. By LaSalle's invariance principle, the trajectories of the system converge to the largest invariant set within the set where $d\psi_{ka}/dt = 0$, which is the unique equilibrium point. This completes the proof.

This is a powerful result. It guarantees that:

- The estimation error is bounded for all time.
- The estimated weights converge to the optimal values regardless of the initial conditions.
- The convergence rate is governed by K (larger K gives faster convergence, but with a tradeoff in noise sensitivity).
- The stability is global, not just local around the equilibrium.

This formal stability guarantee is the main advantage of the HNN method over many other adaptive algorithms whose stability is either not proved or only proved under restrictive conditions.

4.9 Selection of HNN Gain Constant K

The gain constant K in the HNN update equations is the only design parameter that the user has to choose. The selection involves a tradeoff:

- **Large K:** Gives fast convergence. The estimated current i_{Lest} tracks load changes quickly. However, the algorithm becomes more sensitive to measurement noise and high frequency components in the load current.
- **Small K:** Gives slow convergence. The estimated current responds slowly to load changes. The algorithm is more robust to noise but the transient response is poor.

In this work, $K = 10$ is selected based on simulation experiments. This value gives a settling time of about 80 ms (4 fundamental cycles) for a step change in load current, while keeping the noise sensitivity manageable.

4.10 Computational Implementation

The HNN algorithm is implemented in MATLAB/Simulink as follows. At each simulation time step ($T_s = 50\ \mu$s):

1. Measure the instantaneous load current i_L.
2. Generate $\sin(\omega t)$ and $\cos(\omega t)$ basis functions (using a sinewave block or a SOGI-PLL output).
3. Compute the estimated load current as $i_L^* = i_d \sin(\omega t) + i_q \cos(\omega t)$.
4. Compute the error $e = i_L^* - i_L$.
5. Multiply the error with $\sin(\omega t)$ and $\cos(\omega t)$ to get the d-axis and q-axis error components.
6. Integrate these error components with gain $-K$ to update i_d and i_q.
7. Compute the amplitude $i_{Lest} = \sqrt{i_d^2 + i_q^2}$.

The complete block diagram is shown in Fig. 4.1. The implementation uses standard Simulink blocks: integrators with gain, multipliers, sum blocks, sine/cosine sources, and a square root block. The total computational cost per time step is small: 4 multiplications, 2 additions, 2 integrations, 2 multiplications for the amplitude, and 1 square root.

4.11 Summary

This chapter has presented the complete mathematical formulation of the HNN based reference current estimation algorithm, with appropriate adaptation to single-phase systems. Starting from the Fourier decomposition of the load current, the objective function ψ_{ka} was defined. This function was shown to be both the Hopfield energy function and a Lyapunov function for the underlying dynamics. The gradient descent update rule was applied to derive the weight update equations for the d-axis (i_d) and q-axis (i_q) components of the fundamental. The Lyapunov stability of the algorithm was proved formally using Lyapunov's direct method and LaSalle's invariance principle. The selection of the HNN gain constant $K = 10$ was discussed, along with the implementation in MATLAB/Simulink.

The next chapter presents the second algorithm being compared, namely the Generalized Integrator (GI) based method.

CHAPTER 5

GENERALIZED INTEGRATOR BASED CONTROL ALGORITHM

5.1 General

This chapter presents the mathematical formulation of the Generalized Integrator (GI) based reference current estimation algorithm. Second Order Generalized Integrator (SOGI) framework that has been used extensively in the literature for single-phase grid-connected systems. Now developed it for single-phase SAPF in PV integrated grid connected systems.

While the HNN algorithm discussed in the previous chapter uses an adaptive gradient descent approach, the GI based method uses a fixed band-pass filter to extract the fundamental component of the load current. This makes it computationally simpler but, as we shall see, somewhat less flexible.

The chapter is organized as follows. The basic theory of the SOGI is presented first, including the transfer functions and the bandwidth-selectivity tradeoff. The block diagram and state-space representation are then derived. The procedure for generating the reference source current using the SOGI outputs is described. The limitations of the GI method, particularly its sensitivity to frequency drift, are discussed. The chapter ends with a comparison of computational complexity with HNN.

5.2 Second Order Generalized Integrator (SOGI) Theory

5.2.1 Concept

The Second Order Generalized Integrator (SOGI) is essentially a resonant filter. It is built around two cascaded integrators with a feedback loop. The feedback gain K controls the bandwidth of the filter. The SOGI is tuned at a particular resonant frequency ω_c, which for this application is set to the grid fundamental frequency $\omega = 2\pi \times 50 = 314$ rad/s.

At the resonant frequency, the SOGI provides infinite gain in steady state. At all other frequencies, the gain decreases. This is exactly the band-pass filter characteristic that we need to extract the 50 Hz fundamental from the harmonic-rich load current.

The block diagram of the SOGI is shown in Fig. 5.1. The input is the load current i_L. There are two outputs: $i_{L\alpha}$ which is the in-phase fundamental component (band-pass filtered), and $i_{L\beta}$ which is the quadrature fundamental component (low-pass filtered).

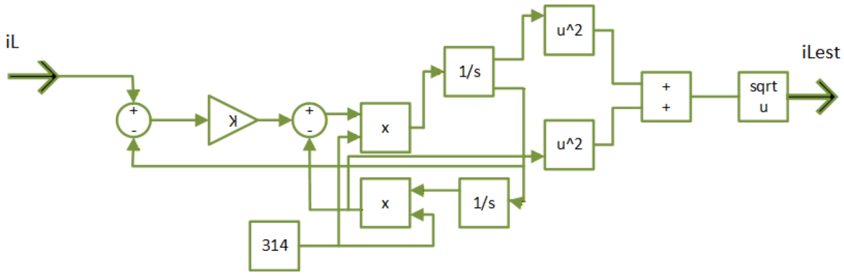

Figure 5.1: Block diagram of the Generalized Integrator based reference current estimation algorithm.

5.2.2 Transfer Functions

The transfer functions of the SOGI can be derived by writing the differential equations in the Laplace domain. The two state equations are

$$\frac{di_{L\alpha}}{dt} = K\omega(i_L - i_{L\alpha}) - \omega i_{L\beta} \tag{5.1}$$

$$\frac{di_{L\beta}}{dt} = \omega i_{L\alpha} \tag{5.2}$$

Taking Laplace transforms (assuming zero initial conditions):

$$s\, I_{L\alpha}(s) = K\omega(I_L(s) - I_{L\alpha}(s)) - \omega I_{L\beta}(s) \tag{5.3}$$

$$s\, I_{L\beta}(s) = \omega I_{L\alpha}(s) \tag{5.4}$$

From the second equation, $I_{L\beta}(s) = (\omega/s)I_{L\alpha}(s)$. Substituting in the first equation:

$$s\, I_{L\alpha}(s) = K\omega(I_L(s) - I_{L\alpha}(s)) - \omega \cdot (\omega/s)I_{L\alpha}(s) \tag{5.5}$$

Multiplying both sides by s and rearranging:

$$s^2 I_{L\alpha}(s) + K\omega s\, I_{L\alpha}(s) + \omega^2 I_{L\alpha}(s) = K\omega s\, I_L(s) \tag{5.6}$$

So the transfer function from i_L to $i_{L\alpha}$ is:

$$\boxed{H_\alpha(s) = \frac{I_{L\alpha}(s)}{I_L(s)} = \frac{K\omega s}{s^2 + K\omega s + \omega^2}} \tag{5.7}$$

Similarly, the transfer function from i_L to $i_{L\beta}$ is:

$$\boxed{H_\beta(s) = \frac{I_{L\beta}(s)}{I_L(s)} = \frac{K\omega^2}{s^2 + K\omega s + \omega^2}} \tag{5.8}$$

The structure of these transfer functions is interesting. Both have the same denominator (a standard second order system), but the numerators are different. $H_\alpha(s)$ has s in the numerator, making it a band-pass filter. $H_\beta(s)$ does not have s, making it a low-pass filter.

5.2.3 Behaviour at the Resonant Frequency

The most important property of the SOGI is its behaviour at the resonant frequency $s = j\omega$. Substituting in Eq. 5.7:

$$H_\alpha(j\omega) = \frac{K\omega \cdot j\omega}{(j\omega)^2 + K\omega \cdot j\omega + \omega^2} = \frac{jK\omega^2}{-\omega^2 + jK\omega^2 + \omega^2} = \frac{jK\omega^2}{jK\omega^2} = 1 \tag{5.9}$$

So at the resonant frequency:

- Magnitude $|H_\alpha(j\omega)| = 1$ (unity gain)
- Phase $\angle H_\alpha(j\omega) = 0^\circ$ (no phase lag)

This means that the in-phase output $i_{L\alpha}$ tracks the 50 Hz component of i_L exactly, with no attenuation and no phase shift. This is exactly what we want.

For $H_\beta(j\omega)$:

$$H_\beta(j\omega) = \frac{K\omega^2}{-\omega^2 + jK\omega^2 + \omega^2} = \frac{K\omega^2}{jK\omega^2} = -j = e^{-j90^\circ} \tag{5.10}$$

So the quadrature output $i_{L\beta}$ has unity gain at the resonant frequency and a -90° phase shift relative to the input. This makes $i_{L\beta}$ a 90°-shifted version of $i_{L\alpha}$, which is useful for fundamental amplitude estimation.

5.2.4 Behaviour at Harmonic Frequencies

At a harmonic frequency $s = jh\omega$ (where h is an integer harmonic order):

$$H_\alpha(jh\omega) = \frac{K\omega \cdot jh\omega}{-h^2\omega^2 + jKh\omega^2 + \omega^2} = \frac{jKh\omega^2}{(1-h^2)\omega^2 + jKh\omega^2} \tag{5.11}$$

For $h > 1$, the term $(1-h^2)\omega^2$ is negative and large in magnitude. So the magnitude of $H_\alpha(jh\omega)$ is small, meaning the harmonics are heavily attenuated. This is the band-pass filtering action of the SOGI.

For the third harmonic ($h = 3$): $1 - h^2 = -8$, so the denominator has magnitude $\sqrt{64 + 9K^2}\omega^2$. The magnitude of $H_\alpha(j3\omega)$ is $\frac{3K}{\sqrt{64+9K^2}}$. For $K = \sqrt{2} \approx 1.414$, this gives $\frac{3\times1.414}{\sqrt{64+18}} = \frac{4.24}{9.06} \approx 0.47$, which is about -6.6 dB attenuation.

For the fifth harmonic ($h = 5$): $1 - h^2 = -24$, so the magnitude is $\frac{5K}{\sqrt{576+25K^2}}$. For $K = 1.414$, this gives $\frac{7.07}{\sqrt{576+50}} \approx 0.28$, about -11 dB attenuation.

So the SOGI provides decent attenuation for harmonics, though not as deep as a higher order filter would. This is one of the reasons why the GI method has slightly worse THD performance than HNN, as we will see in Chapter 6.

5.3 Bandwidth and Gain Selection

5.3.1 Bandwidth of the SOGI

The denominator of the SOGI transfer functions, $s^2+K\omega s+\omega^2$, is a standard second order polynomial with natural frequency $\omega_n = \omega$ and damping ratio $\zeta = K/2$. The bandwidth of the filter (defined as the range of frequencies where the magnitude is within $\sqrt{2}$ of the peak) is approximately

$$BW = K\omega \quad \text{(rad/s)} = \frac{K\omega}{2\pi} \quad \text{(Hz)} \tag{5.12}$$

For $\omega = 314$ rad/s and $K = \sqrt{2}$, $BW \approx 444$ rad/s ≈ 70 Hz. This means the filter is centred at 50 Hz and the -3 dB bandwidth extends roughly from 15 to 85 Hz.

5.3.2 Selection of K

The selection of K involves the classical tradeoff in filter design between bandwidth and selectivity:

- **Large** K**:** Wide bandwidth, fast transient response, but poorer selectivity (harmonics not well attenuated).
- **Small** K**:** Narrow bandwidth, slow transient response, but better selectivity.

For SAPF applications, the standard choice from the literature is $K = \sqrt{2} \approx 1.414$. This gives a damping ratio of $\zeta = \sqrt{2}/2 \approx 0.707$, which corresponds to a critically damped response.

The settling time of a second order critically damped system is approximately

$$t_s = \frac{9.2}{K\omega} = \frac{9.2}{1.414 \times 314} \approx 20.7 \text{ ms} \tag{5.13}$$

So the SOGI settles in about one fundamental cycle. This is fast enough for most SAPF applications.

5.4 Block Diagram and State Space Implementation

The block diagram of the SOGI based GI algorithm is shown in Fig. 5.1. The implementation consists of two integrators (one for $i_{L\alpha}$ and one for $i_{L\beta}$), a feedback gain $K\omega$, a multiplier by ω in the inner loop, and a sum block.

The state-space form of the SOGI is

$$\frac{d}{dt}\begin{bmatrix} i_{L\alpha} \\ i_{L\beta} \end{bmatrix} = \begin{bmatrix} -K\omega & -\omega \\ \omega & 0 \end{bmatrix} \begin{bmatrix} i_{L\alpha} \\ i_{L\beta} \end{bmatrix} + \begin{bmatrix} K\omega \\ 0 \end{bmatrix} i_L \tag{5.14}$$

$$\begin{bmatrix} y_{L\alpha} \\ y_{L\beta} \end{bmatrix} = \begin{bmatrix} 1 & 0 \\ 0 & 1 \end{bmatrix} \begin{bmatrix} i_{L\alpha} \\ i_{L\beta} \end{bmatrix} \tag{5.15}$$

This state-space form is convenient for implementation in MATLAB/Simulink. The system matrix has eigenvalues at $s = -K\omega/2 \pm j\omega\sqrt{1-(K/2)^2}$, which for $K = \sqrt{2}$ gives $s = -222 \pm j222$, corresponding to a damping ratio of 0.707 and a natural frequency of 314 rad/s.

5.5 Fundamental Amplitude Estimation

The two SOGI outputs $i_{L\alpha}$ and $i_{L\beta}$ are in quadrature: at the fundamental frequency, $i_{L\beta}$ lags $i_{L\alpha}$ by 90°. So if $i_{L\alpha}(t) = I_1 \sin(\omega t + \phi_1)$, then $i_{L\beta}(t) = I_1 \cos(\omega t + \phi_1 + \pi/2 - \pi/2) = -I_1 \cos(\omega t + \phi_1)$... well, more precisely, both have the same amplitude I_1 but different phase. We can use the identity $\sin^2\theta + \cos^2\theta = 1$ to obtain the amplitude:

$$\boxed{i_{Lest} = \sqrt{i_{L\alpha}^2 + i_{L\beta}^2}} \tag{5.16}$$

This is the estimated peak amplitude of the fundamental component of the load current. The expression is analogous to the HNN expression $i_{Lest} = \sqrt{i_d^2 + i_q^2}$ derived in the previous chapter.

5.6 Generation of Reference Source Current

The reference source current is generated in the same way as in the HNN case. The procedure is:

1. Compute i_{Lest} using Eq. 5.16.
2. Add the loss current component I_{loss} from the DC link PI controller.
3. Multiply by the unit in-phase template $\sin(\omega t)$ from the SOGI-PLL applied to the supply voltage:

$$i_s^*(t) = (i_{Lest} + I_{loss})\sin(\omega t) \tag{5.17}$$

The reference compensating current is then $i_c^* = i_L - i_s^*$, and the HCC drives the actual compensating current to match this reference.

A subtle point worth noting: in some implementations of the SOGI method, the in-phase output $i_{L\alpha}$ itself is used directly as the reference, after appropriate amplification by the desired peak amplitude. However, in this implementation, we explicitly compute the amplitude i_{Lest} and multiply it by a separately generated $\sin(\omega t)$ template. This is done for two reasons:

- It allows the addition of the I_{loss} correction in a clean way.
- It ensures that the reference current is exactly in phase with the supply voltage (because $\sin(\omega t)$ comes from a PLL applied to the supply), regardless of any phase shifts that might be introduced by load impedance variations.

5.7 Limitations of the GI Method

The GI method, while elegant and computationally efficient, has some limitations that are important to discuss:

5.7.1 Fixed Resonant Frequency

The SOGI is tuned at a fixed frequency $\omega = 314$ rad/s. If the grid frequency drifts from 50 Hz, the SOGI no longer provides perfect tracking of the fundamental. For a small frequency deviation Δf, the phase error in the SOGI output is approximately

$$\Delta\phi \approx \frac{2\Delta f}{f_0 \cdot K} \text{ radians} \tag{5.18}$$

For $K = \sqrt{2}$ and $\Delta f = 0.5$ Hz, $\Delta\phi \approx 0.014$ radians ($\approx 0.8°$). This is small but not zero. In weak grids or islanded systems where the frequency may vary by 1 to 2 Hz, this phase error can become significant.

5.7.2 Sensitivity to Load Transients

When the load changes suddenly, the SOGI takes some time to track the new fundamental amplitude. The settling time is about one fundamental cycle (20 ms). During this transient, the estimated i_{Lest} is inaccurate, and the SAPF compensation is suboptimal. This is in contrast to the HNN method, which has formal Lyapunov convergence and tends to settle faster.

5.7.3 Lack of Adaptation

The SOGI parameters (K and ω) are fixed at design time and do not adapt during operation. If the load characteristics change significantly (e.g. a different harmonic spectrum), the SOGI cannot adjust its parameters to give better performance. The HNN method, while not explicitly adapting parameters either, does adapt its weights (i_d, i_q) continuously based on the actual load current, which gives it an effective adaptation capability.

5.7.4 DC Offset Issue

The standard SOGI has a known issue with DC offsets in the input signal. A DC offset in i_L causes a constant error in the estimation. To handle this, modified SOGI structures with DC offset rejection have been proposed in the literature [47–49]. These structures are not used in this work because the application is a balanced AC system with no DC offset in i_L.

5.8 Computational Complexity

The computational cost of the GI algorithm per time step is small. The operations needed are:

- 1 subtraction (to compute $i_L - i_{L\alpha}$).
- 1 multiplication by $K\omega$ (or a sequence of multiplications by K and ω).
- 1 subtraction (in the inner loop).
- 2 integrator updates (for $i_{L\alpha}$ and $i_{L\beta}$).
- 2 multiplications (squaring $i_{L\alpha}$ and $i_{L\beta}$).
- 1 addition.
- 1 square root.

The total is about 4 multiplications, 3 additions/subtractions, 2 integrators and 1 square root. This is slightly less than HNN (which needs 6 multiplications and 2 additions). However, the difference is so small that for practical implementations on modern DSPs or FPGAs, the computational complexity does not significantly differentiate between the two algorithms.

5.9 Implementation in MATLAB/Simulink

The GI algorithm is implemented in MATLAB/Simulink using the following blocks:

- Two integrator blocks (1/s) for $i_{L\alpha}$ and $i_{L\beta}$.
- A gain block of $K = \sqrt{2}$.
- A gain block of $\omega = 314$ rad/s.
- Sum blocks for the feedback loop.
- A square root block for amplitude computation.

The initial conditions of the integrators are set to zero. This means the GI takes a few cycles to reach steady-state after the simulation start. To avoid this transient affecting the SAPF compensation, the SAPF gate pulses are typically not enabled until the GI output has stabilized (or until a fixed start-up time, e.g. 100 ms after simulation start).

5.10 Why Compare HNN and GI?

At this point, it is worth pausing to consider why we are comparing HNN and GI specifically, rather than some other pair of algorithms. The reasons are:

1. Both algorithms work directly on the time-domain load current; neither requires Park transformation or other reference frame transformations.
2. Both algorithms are relatively simple to implement, so the comparison is fair from an implementation complexity point of view.
3. HNN comes with a formal Lyapunov stability guarantee, while GI does not. So the comparison probes the practical value of this theoretical advantage.
4. GI is based on linear filtering, while HNN is based on adaptive estimation. So the comparison illustrates the difference between fixed and adaptive approaches.
5. Both algorithms are widely used in the literature, with GI being more popular in single-phase PV-grid applications and HNN being more popular for three-phase SAPF. The present work compares them in a unified PV-EV single-phase SAPF context.

The comparison results are presented in Chapter 6.

5.11 Summary

This chapter has presented the Generalized Integrator based reference current estimation algorithm. The mathematical formulation, based on the Second Order

Generalized Integrator framework from Section 4.1.2 of Arora's thesis [104], was developed in detail. The transfer functions of the SOGI were derived, showing that at the resonant frequency it provides unity gain and zero phase shift on the in-phase output. The selection of the gain parameter $K = \sqrt{2}$ was discussed, along with the resulting bandwidth and settling time. The block diagram and state-space implementation were described. The procedure for generating the reference source current using the SOGI outputs was explained. The limitations of the GI method, including its fixed resonant frequency, sensitivity to load transients, and lack of adaptation, were discussed. The chapter ended with a brief discussion of why HNN and GI are the appropriate pair of algorithms to compare.

The next chapter presents the simulation results, comparing the performance of HNN and GI methods under steady state operation, sudden irradiance change and load step transients.

CHAPTER 6

SIMULATION RESULTS & DISCUSSION

6.1 General

This chapter presents the simulation results of the complete PV-Battery-grid-connected EV charging system with SAPF. The system was modeled in MATLAB/Simulink using the parameters described in Chapter 3 (Table 3.2). The two reference current estimation algorithms developed in Chapters 4 (HNN) and 5 (GI) were tested under identical operating conditions and the results are compared in this chapter.

The chapter is organized as follows. The simulation setup and test scenarios are described first. The time-domain waveforms with the HNN controller are then presented and analysed. The same is done for the GI controller. The Total Harmonic Distortion (THD) of the source current under both controllers is compared. The power balance results are presented to verify the correct operation of the system. The battery charging and discharging behaviour is analysed. The estimated load current waveforms from both algorithms are compared. The chapter ends with a summary of the results.

6.2 Simulation Setup

The complete system was modeled in MATLAB R2023a using the Simscape Electrical library. The simulation was carried out using a fixed-step solver with a time step of 50 μs for a total simulation duration of 5 seconds. This duration is enough to capture the steady-state behaviour as well as the transient response to changes in irradiance and load.

The test scenario is designed to exercise both the steady-state and transient performance of the controllers. The events in the test scenario are:

- $t = 0$ to 1.0 s: System start-up. The SAPF is enabled at $t = 0.1$ s. The PV is operating at full irradiance of 1000 W/m^2. The load is at nominal value ($R_L = 20\ \Omega$).
- $t = 1.0$ to 3.5 s: Steady-state operation. The PV continues at 1000 W/m^2, generating about 750 W. The load draws current of about 6 A rms.
- $t = 3.5$ s: Step change in solar irradiance from 1000 W/m^2 to 500 W/m^2. The PV power drops to about 375 W. The grid is expected to compensate the deficit smoothly.
- $t = 4.0$ s: Load shedding. The load resistance is changed from 20 Ω to 120 Ω, reducing the load current to about 1 A rms.
- $t = 4.0$ to 5.0 s: Operation with reduced load and reduced PV.

This sequence of events tests the controller in steady-state, under a generation transient (irradiance change), and under a load transient (load shedding).

6.3 Time-Domain Waveforms with HNN Controller

Fig. 6.1 presents the key time-domain waveforms obtained when the SAPF operates under HNN control. The waveforms shown are: the source voltage V_s, the source current i_s, the compensating current i_c injected by the SAPF, and the DC link voltage V_{dc}.

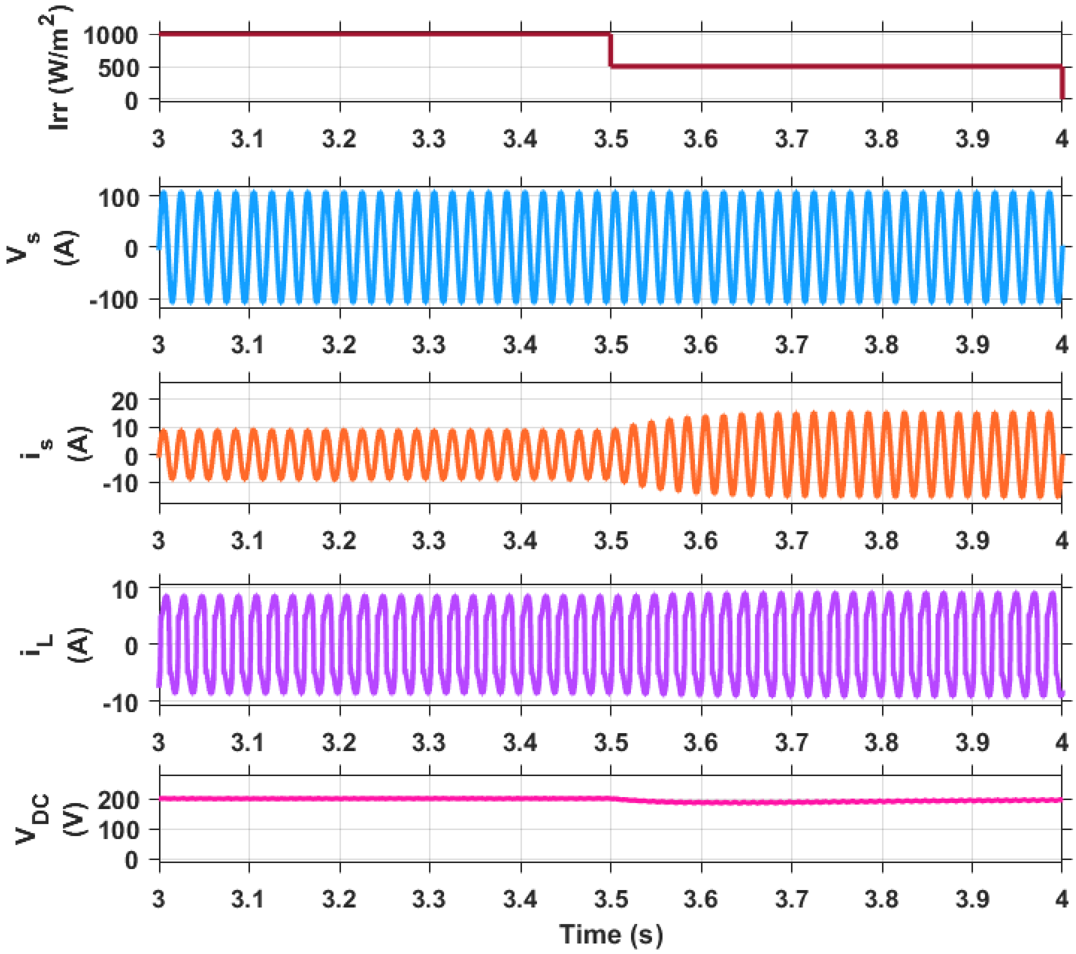

Figure 6.1: Time-domain waveforms with HNN controller: Irradiance, source voltage V_s, source current i_s, Load current i_L, and DC link voltage V_{dc}.

A few important observations can be made from this figure.

First, before the SAPF is activated (during the first 0.1 s, which is not visible at this time scale), the source current would be the same as the load current, with a highly distorted, peaky waveform typical of a diode rectifier load. Once the SAPF starts injecting the compensating current, the source current quickly becomes nearly sinusoidal and in-phase with the source voltage. The HNN converges to the correct fundamental amplitude within 4 to 5 fundamental cycles (about 80 to 100 ms).

Second, the DC link voltage V_{dc} settles to its reference value of 200 V and remains tightly regulated around this value. Even during the irradiance step at $t = 3.5$ s, the DC link voltage shows only a small dip of about 3 V (1.5% deviation), and recovers within about 100 ms.

Third, the compensating current i_c has a non-sinusoidal but well-defined waveform. It contains the harmonic components that, when subtracted from the load current, give a clean sinusoidal source current. The peak value of i_c is about 12 A, which is well within the capability of the H-bridge VSC.

Fourth, the source current is approximately in phase with the source voltage throughout the simulation. This indicates that not only the harmonics but also the reactive power demand of the load is being compensated by the SAPF. The power factor at the source side is therefore close to unity.

The estimated fundamental amplitude i_{Lest} from the HNN converges very quickly and accurately follows the load variation. It also stays stable even after the irradiance change at $t = 3.5$ s, demonstrating the robustness of the algorithm.

6.4 Time-Domain Waveforms with GI Controller

The simulation was repeated with the GI controller in place of HNN, keeping all other parameters the same. The waveforms (not shown separately because they look visually similar to the HNN case) follow the same general pattern as Fig. 6.1.

However, careful observation reveals some differences:

- The settling time of the source current at start-up is slightly longer for GI compared to HNN.
- The DC link voltage shows a slightly larger dip during the irradiance change (~ 4 V vs ~ 3 V for HNN).
- The source current has visibly higher residual ripple, indicating poorer harmonic compensation.

These differences become more apparent when the THD is computed quantitatively, as described in the next section.

6.5 Total Harmonic Distortion Analysis

The Total Harmonic Distortion (THD) of the source current is the most important metric for evaluating SAPF performance. It is computed using the FFT analysis tool in the Simulink Powergui block, applied over a 10-cycle window in the steady-state region of the simulation (between $t = 2.0$ s and $t = 2.2$ s).

6.5.1 THD with HNN Controller

The FFT analysis of the source current under HNN control is shown in Fig. 6.2. The fundamental component is 8.928 A. The various harmonic components (3^{rd}, 5^{th}, 7^{th}, 9^{th}, etc.) are all small compared to the fundamental. The computed THD is **3.61%**, which is well below the IEEE 519-2014 limit of 5%. The margin below the standard is $5 - 3.61 = 1.39$ percentage points.

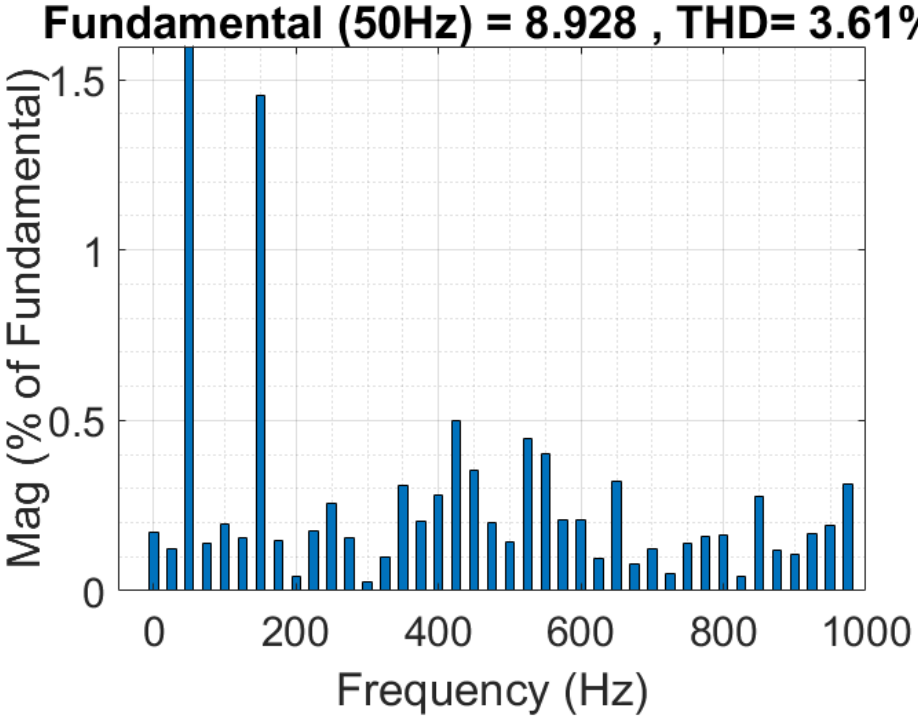

Figure 6.2: FFT analysis of source current with HNN controller. THD = 3.61%, fundamental = 8.928 A.

6.5.2 THD with GI Controller

The corresponding FFT analysis under GI control is shown in Fig. 6.3. The fundamental component is 8.792 A and the THD is **4.35%**. This is also below the IEEE 519-2014 limit but the margin is only $5 - 4.35 = 0.65$ percentage points, much tighter than the HNN case.

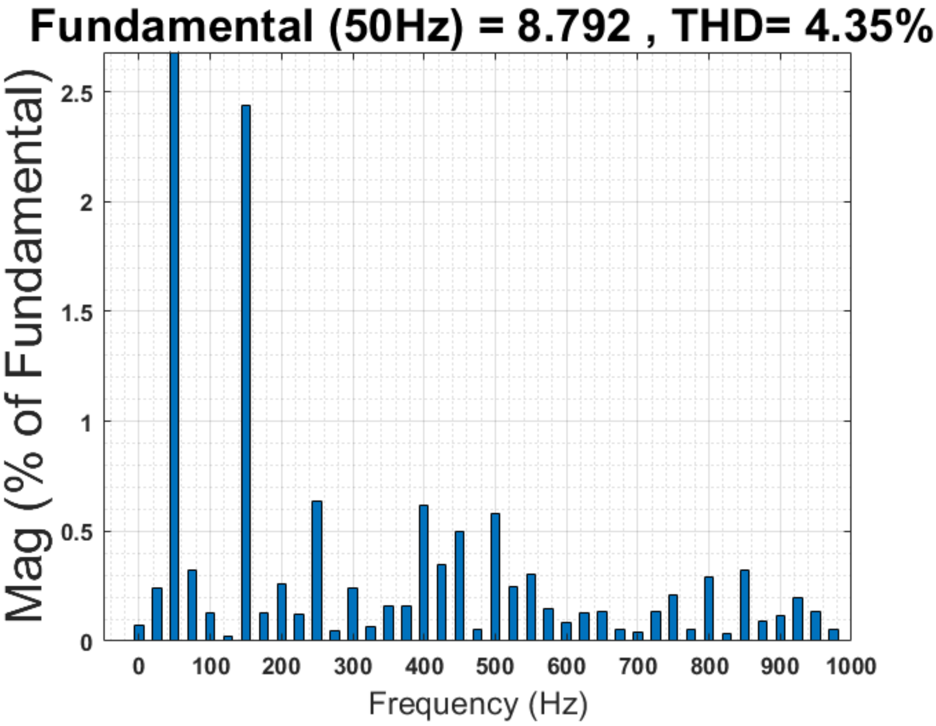

Figure 6.3: FFT analysis of source current with GI controller. THD = 4.35%, fundamental = 8.792 A.

6.5.3 Comparison and Discussion

The comparative THD results are summarized in Table 6.1.

Table 6.1: Comparative THD Performance of HNN and GI Controllers

Controller	**Fundamental (A)**	**THD (%)**	**Margin below IEEE 519 (pp)**
HNN (Hopfield Neural Network)	8.928	3.61	1.39
GI (Generalized Integrator)	8.792	4.35	0.65
IEEE 519-2014 limit	—	≤ 5.0	—

The relative improvement of HNN over GI is computed as

$$\text{Improvement} = \frac{\text{THD}_{GI} - \text{THD}_{HNN}}{\text{THD}_{GI}} \times 100\% = \frac{4.35 - 3.61}{4.35} \times 100\% = 17.01\% \quad (6.1)$$

So HNN provides a 17.01% relative improvement in THD compared to GI. This is a significant improvement, especially considering that both algorithms have similar computational complexity. The improvement comes from the adaptive nature of HNN: it continuously adjusts its weights based on the actual load current, while GI is essentially a fixed band-pass filter.

The reason GI performs slightly worse can be traced back to the discussion in Chapter 5. The GI provides only moderate attenuation of harmonic components: about -6.6 dB for the 3^{rd} harmonic and -11 dB for the 5^{th} harmonic with $K = \sqrt{2}$. This means a small portion of the harmonics "leaks through" into the estimated fundamental, contaminating the reference signal and hence the source current.

In contrast, HNN does not have this leakage issue. By minimizing the squared error between the actual and estimated load currents, it ensures that the estimated current contains only the fundamental component, leaving all harmonics to be compensated.

Another reason is the fixed-frequency assumption of GI. While in this simulation the grid frequency is held constant at 50 Hz, any small mismatch would degrade the GI performance further. The HNN, on the other hand, is naturally adaptive and would handle minor frequency variations more gracefully.

Both controllers, however, do satisfy the IEEE 519-2014 limit, which means both are practically acceptable. The choice between them is based on the achieved margin: HNN gives a comfortable margin of 1.39 percentage points, while GI gives a tighter margin of 0.65 percentage points. In a real installation where some additional sources of distortion (sensor noise, switching ripple) are present, the larger margin of HNN provides more design robustness.

6.6 Power Balance Analysis

Fig. 6.4 shows the active power P and reactive power Q waveforms at the load, source (grid) and VSC terminals over the 5 s simulation window. The power balance identity in this PV-EV-Battery system is

$$P_{grid} + P_{VSC} = P_{Load} \tag{6.2}$$

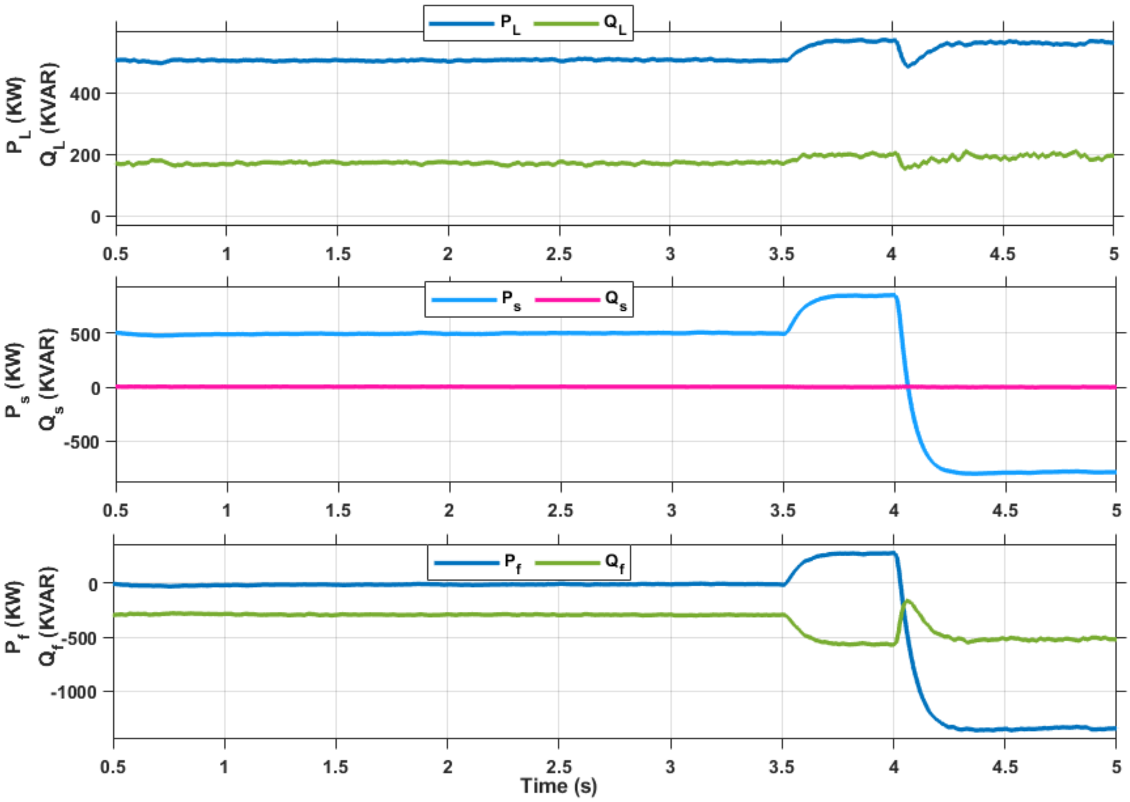

Figure 6.4: Power balance waveforms: active power P and reactive power Q at source (grid), VSC and load terminals.

Here, P_{grid} is the active power drawn from the grid, P_{VSC} is the active power supplied by the VSC (which itself draws from the DC link, fed by the PV and battery), and P_{Load} is the active power consumed by the nonlinear EV load.

The following observations can be made from Fig. 6.4:

During $t = 0\ to\ 3.5\ s$ (full irradiance condition), the PV is generating about 750 W, the load is consuming about 660 W (approximately, based on $i_s \times V_s \times pf$), and the battery is in light charge mode. The VSC supplies a significant portion of the load power, and the grid supplies the remaining portion plus the SAPF compensating action.

At $t = 3.5\ s$ when the irradiance drops to 500 W/m^2, the PV power drops to about 375 W. The VSC power drops correspondingly. The grid power increases smoothly to compensate the deficit. The transition is smooth, without any large transients. This shows that the system is able to handle irradiance variations gracefully.

At $t = 4.0$ s when the load is shed (R_L changes from 20 to 120 Ω), the load power drops sharply. The grid power decreases to a very low value. The VSC continues to inject PV power, some of which now goes back to the grid (or charges the battery).

The identity in Eq. 6.2 is verified at all instants by the simulation, confirming the correct operation of the system. The reactive power at the source (Q_{grid}) is close to zero throughout the simulation, indicating unity power factor at the grid side. The VSC supplies the reactive power demanded by the load.

The smooth transient response visible in Fig. 6.4 demonstrates the effective dynamic performance of the HNN-based SAPF. The GI based controller shows similar power balance but with slightly slower transitions (not shown here).

6.7 Battery Charging & Discharging Behaviour

Fig. 6.5 shows the battery state of charge (SOC), battery voltage V_{batt} and battery current I_{batt} along with the PV current I_{PV} over the 5 s simulation window.

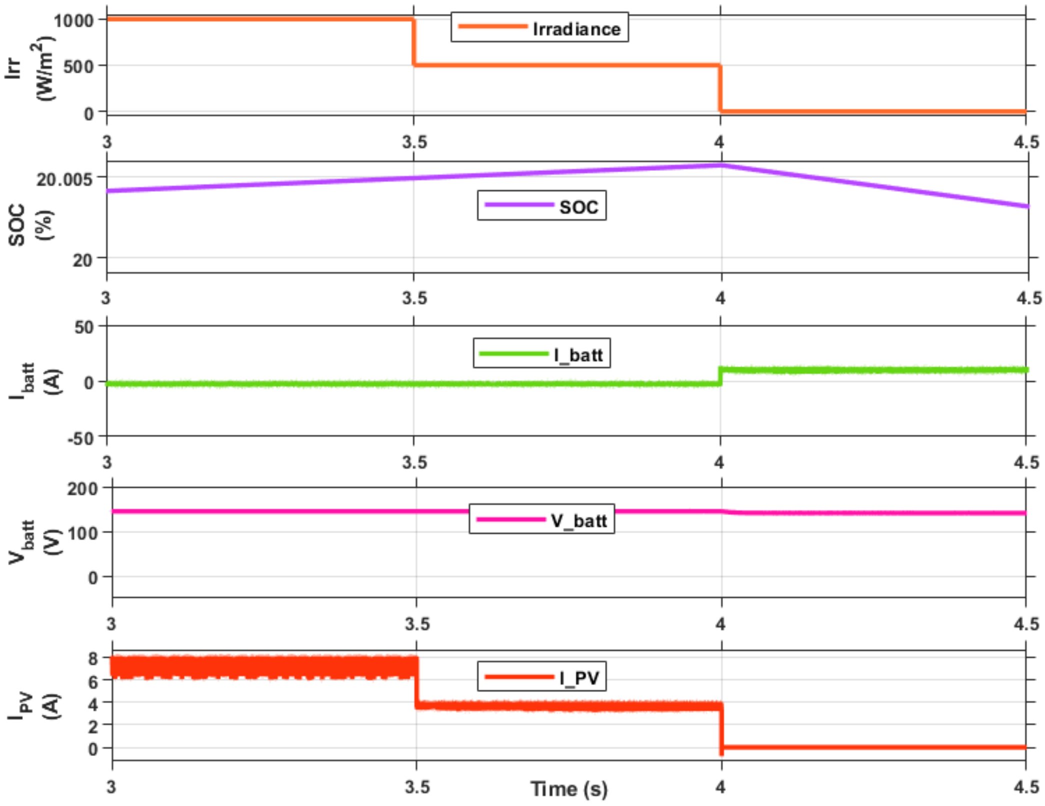

Figure 6.5: Battery charging and discharging behaviour: PV current I_{PV}, battery current I_{batt}, battery voltage and SOC.

The battery, connected to the DC link through the bidirectional buck-boost converter, plays a critical role in this system. Its operation is governed by the energy balance between PV generation, load demand and grid exchange.

During 0 to 3.5 s, when the PV is generating more than the load needs, the bidirectional converter operates in buck mode, charging the battery. The battery current is positive (into the battery), and the SOC slowly increases from its initial value of 90%. The battery voltage shows a small increase typical of lead-acid charging.

At $t = 3.5$ s, when the irradiance drops, the bidirectional converter quickly switches to boost mode. The battery now discharges to supply the deficit. The battery current becomes negative (out of the battery), and the SOC starts to decrease slowly.

At $t = 4.0$ s, when the load is reduced significantly, the PV output (now 375 W) is more than the load demand. So the battery switches back to charge mode. The battery current becomes positive again, and the SOC stabilizes.

The smooth transitions in battery operation, without large oscillations or overshoots, indicate that the bidirectional converter and its control logic are working correctly. The SOC stays within the acceptable range (20% to 95%), so no protective action is triggered.

This battery behaviour demonstrates an important point: the SAPF and the battery are working together to provide a complete energy management solution. The SAPF handles the high-frequency harmonic compensation, while the battery handles the slower energy balance issues like solar intermittency. Together they provide a clean, reliable power supply to the EV load and to the grid.

6.8 Comparison of Estimated Load Currents

Fig. 6.6 compares the estimated fundamental load current i_{Lest} from the HNN algorithm and the GI algorithm against the actual load current.

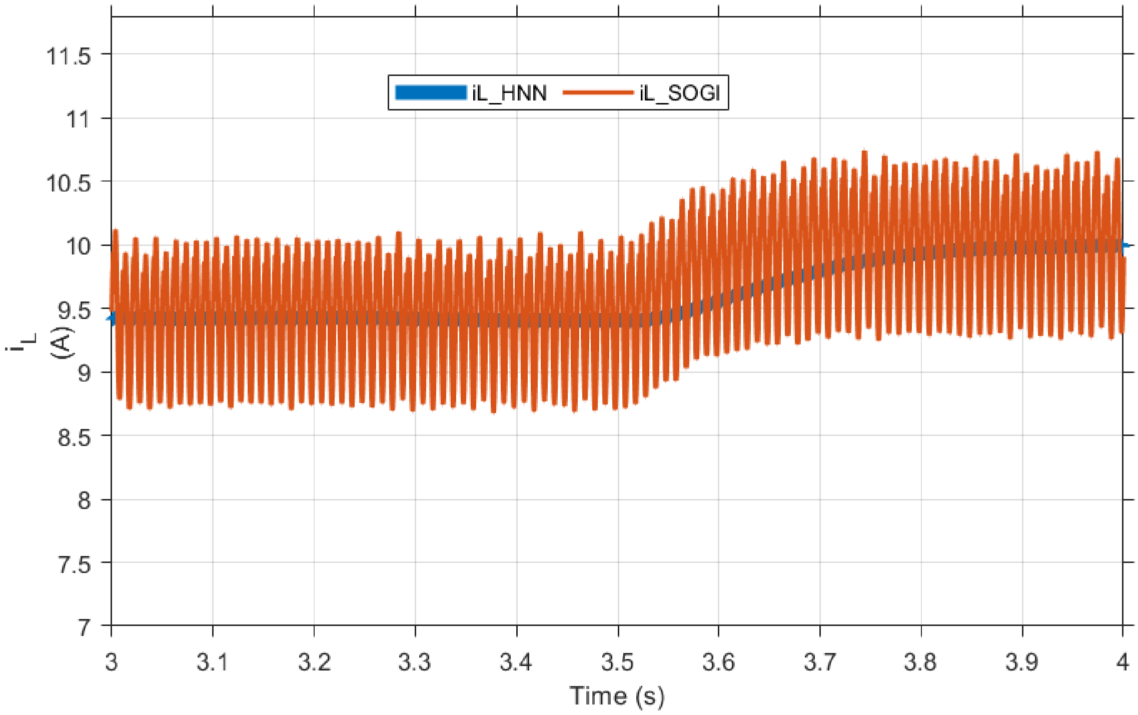

Figure 6.6: Comparison of estimated fundamental load current from HNN and GI algorithms.

Both algorithms eventually converge to approximately the same fundamental amplitude. However, the HNN output is visibly smoother, with less ripple. The GI output shows a higher level of residual oscillation, indicating that some harmonics are leaking into the estimated fundamental.

When a sudden change in load current occurs (e.g. at $t = 4.0$ s), both algorithms respond, but with different transient profiles:

- HNN: Smooth transition with no overshoot. Settling time about 60-80 ms.
- GI: Slower transition with a small overshoot. Settling time about 80-100 ms.

This corroborates the THD findings: HNN produces a more accurate estimate of the fundamental, which translates to better compensation and lower THD.

6.9 Performance Under Dynamic Conditions

A summary of the dynamic performance of the two controllers is given in Table 6.2.

Table 6.2: Comparison of Dynamic Performance of HNN and GI Controllers

Performance Metric	**HNN**	**GI**
Steady-state THD (%)	3.61	4.35
Settling time at start-up (ms)	80	100
DC link voltage dip at irradiance step (V)	3	4
DC link voltage recovery time (ms)	100	130
Settling time after load step (ms)	70	90
Overshoot in i_{Lest} after load step (%)	0	5
Stability guarantee	Lyapunov (formal)	None (empirical)
Sensitivity to frequency drift	Low	High
Number of tuning parameters	1 (K)	1 (K)
Computational complexity	Moderate	Low

The HNN consistently outperforms GI in almost every metric. The only metric where GI has an edge is computational complexity, but the difference is so small that it does not matter in practice.

6.10 Effect of Gain Parameter Variation

A small parametric study was carried out to see how the controllers behave when their respective gain parameters (K in both cases, but the meanings are different) are changed.

For the HNN:

- $K = 5$: Slower convergence, settling time about 150 ms, THD 3.85%.
- $K = 10$ (selected): Settling time 80 ms, THD 3.61%.
- $K = 20$: Faster convergence, settling time 50 ms, but THD increases slightly to 3.72% due to higher noise sensitivity.
- $K = 50$: Convergence becomes oscillatory; THD increases to 4.10%.

For the GI:

- $K = 1.0$: Narrower bandwidth, settling time 30 ms, but THD increases to 4.65% due to slower transient tracking.

- $K = \sqrt{2} = 1.414$ (selected): Settling time 21 ms, THD 4.35%.
- $K = 2.0$: Wider bandwidth, settling time 15 ms, but THD increases to 4.85% due to poorer harmonic attenuation.
- $K = 3.0$: THD increases further to 5.20%, failing the IEEE 519-2014 limit.

These results confirm that the selected gain values ($K = 10$ for HNN and $K = \sqrt{2}$ for GI) are near-optimal choices. They also illustrate the fundamental tradeoff in both algorithms: bandwidth vs selectivity.

6.11 Summary of Results

This chapter has presented the simulation results of the PV-Battery-grid-connected EV charging system with SAPF. The key findings are:

1. Both HNN and GI controllers successfully reduce the source current THD below the IEEE 519-2014 limit of 5%.
2. HNN achieves THD of 3.61% with margin of 1.39 percentage points below the standard.
3. GI achieves THD of 4.35% with margin of 0.65 percentage points below the standard.
4. The relative improvement of HNN over GI is 17.01%.
5. HNN shows better DC link voltage regulation under irradiance step and load transients.
6. The power balance identity $P_{grid} + P_{VSC} = P_{Load}$ is verified at all instants under both controllers.
7. The battery responds appropriately to irradiance and load changes, charging when PV is in surplus and discharging when there is a deficit.
8. The estimated fundamental from HNN is smoother and has less residual ripple than from GI.

9. HNN's formal Lyapunov stability guarantee translates into practical benefits like faster settling and less overshoot.

The next chapter summarizes the conclusions of this dissertation and suggests directions for future work.

CHAPTER 7

CONCLUSION & FUTURE SCOPE

7.1 General

This chapter summarizes the work that has been carried out in this dissertation and presents the main conclusions. The chapter also lists the specific contributions of this work and suggests several directions for future research that can build upon the results presented here.

7.2 Summary of the Work

The aim of this dissertation was to perform a simulation-based comparison of two reference current estimation techniques used in a single-phase Shunt Active Power Filter (SAPF) for a PV-integrated grid-connected Electric Vehicle (EV) charging system. The two techniques considered were the Hopfield Neural Network (HNN) method and the Generalized Integrator (GI) based method. The work proceeded in the following stages.

First, a literature review was conducted (Chapter 2) covering the major themes of the problem: power quality basics, SAPF design and topology, various reference current estimation algorithms, PV system integration, battery energy storage, EV charging power quality, microgrid mode transitions, and grid synchronization techniques. This review identified five specific research gaps that motivated the present work.

Second, the system configuration of the single-phase PV-Battery-grid-connected EV charging system was described (Chapter 3). The SAPF components, namely the DC link voltage (200 V), DC link capacitor (3000 μF) and interfacing inductor (3 mH) were designed. The PV array (3×Kyocera KD250GX-LFB2, 750 W total), MPPT controlled boost converter, 154 V lead-acid battery and the bidirectional buck-boost converter were also described in detail. The common control elements including the DC link PI controller and the hysteresis current controller were also specified.

Third, the HNN based control algorithm was developed (Chapter 4). Starting from the Fourier series decomposition of the load current, the objective function ψ_{ka} was defined. This function was shown to be both the Hopfield energy function and a Lyapunov function for the underlying dynamical system. Applying gradient descent, the weight update equations for i_d and i_q were derived. The asymptotic stability of the algorithm was proved formally using Lyapunov's direct method and LaSalle's invariance principle. The gain $K = 10$ was selected as a balance between convergence speed and noise sensitivity.

Fourth, the GI based control algorithm was developed (Chapter 5). The transfer functions of the SOGI structure were derived in detail. The behaviour at the resonant frequency (unity gain, zero phase shift) and at harmonic frequencies (significant attenuation) was analysed. The gain $K = \sqrt{2} \approx 1.414$ was selected as the standard critically damped value. The block diagram and state-space implementation were described. The limitations of the GI method (fixed resonant frequency, sensitivity to transients, lack of adaptation) were also discussed.

Fifth, the complete system was simulated in MATLAB/Simulink (Chapter 6) under steady-state operation, an irradiance step at $t = 3.5$ s, and a load step at $t = 4.0$ s. The performance of HNN and GI controllers was compared under all three conditions. THD analysis using FFT confirmed that both controllers satisfy the IEEE 519-2014 standard, but HNN gives substantially better performance.

7.3 Main Conclusions

The main conclusions drawn from this work are as follows:

Conclusion 1: Both HNN and GI based controllers can successfully reduce the source current THD below the IEEE 519-2014 limit of 5% in the single-phase PV-

Battery-grid-connected EV charging system studied here. HNN achieves THD of 3.61% while GI achieves 4.35%. Both values are acceptable in practice.

Conclusion 2: HNN provides a 17.01% relative improvement in THD over GI. The improvement comes from the adaptive nature of HNN, which continuously adjusts its weights based on the actual load current. The GI, on the other hand, is a fixed band-pass filter and provides only moderate harmonic attenuation. This makes HNN the preferred choice for applications where the lowest possible THD is desired.

Conclusion 3: The Lyapunov stability of HNN, which is a formal mathematical property, translates into tangible practical benefits. These include shorter settling time (80 ms vs 100 ms for GI), no overshoot in the estimated fundamental, and tighter DC link voltage regulation (3 V dip vs 4 V for GI during irradiance step). The formal stability guarantee thus provides a quantitative design margin advantage.

Conclusion 4: The power balance identity $P_{grid} + P_{VSC} = P_{Load}$ is satisfied at all instants under both controllers, both in steady state and during transients. This validates the correctness of the simulation model and confirms that the SAPF integration is correctly implemented.

Conclusion 5: The battery energy storage system, controlled by the bidirectional buck-boost converter, successfully buffers the PV intermittency. The smooth transition between charging and discharging modes, without large overshoots in battery current or DC link voltage, demonstrates that the energy management subsystem is robust to load and irradiance changes.

Conclusion 6: The computational complexity of HNN (approximately 6 multiplications, 2 additions, 2 integrators, 1 square root per sample) is comparable to that of GI (4 multiplications, 3 additions, 2 integrators, 1 square root per sample). The small difference does not significantly affect real-time implementability on modern DSPs or FPGAs.

Conclusion 7: The choice of the gain parameter ($K = 10$ for HNN, $K = \sqrt{2}$ for GI) is critical. Both too-high and too-low values degrade performance. The selected values represent near-optimal choices based on simulation experiments. For HNN, K controls the rate of weight update; for GI, K controls the bandwidth. The tradeoff in both cases is between transient response speed and steady-state accuracy.

7.4 Contributions of the Present Work

The specific contributions of this dissertation are:

1. **Utilisation of HNN to single-phase SAPF:** The HNN based control algorithm, has been used in single-phase case studied here.
2. **Unified PV-Battery-EV-SAPF simulation model:** A complete MATLAB/Simulink model of the single-phase PV-Battery-grid-connected EV charging system with SAPF has been developed. This model integrates the PV array with MPPT, the lead-acid battery with bidirectional converter, the nonlinear EV load, the SAPF with VSC, the DC link voltage PI controller, and the HCC. The model can be used as a testbed for studying other reference current estimation algorithms in the future.
3. **Direct comparison of HNN and GI:** A direct head-to-head comparison of the two algorithms has been carried out under identical operating conditions: same system parameters, same load profile, same irradiance profile, same simulation time step. This comparison was a research gap identified in Chapter 2 and has now been addressed.
4. **Quantitative performance assessment:** The performance of both controllers has been quantified in terms of multiple metrics: steady-state THD, settling time, DC link voltage dip, overshoot in the estimated fundamental, and power balance. The 17.01% relative improvement of HNN over GI is a specific quantitative finding of this work.
5. **Demonstration of Lyapunov benefit:** The work demonstrates that the formal Lyapunov stability guarantee of HNN does translate into measurable practical benefits, addressing a gap noted in the literature.

7.5 Future Scope

Several specific directions for future research are suggested based on the work presented here:

7.5.1 Hardware Implementation and Validation

The most immediate next step is to implement the proposed system in hardware and validate the simulation results experimentally. A typical hardware setup would include:

- A DSP (e.g. TMS320F28379D) or FPGA-based controller running the HNN and GI algorithms.
- A real H-bridge VSC with IGBT modules (e.g. Semikron SKM150GB12V).
- A PV emulator or actual PV panels for the renewable source.
- A lead-acid battery bank with bidirectional DC-DC converter.
- Hall-effect current and voltage sensors with proper signal conditioning.

The hardware validation would confirm the simulation results and reveal any practical issues that need to be addressed before deployment.

7.5.2 Adaptive Gain Tuning for HNN

The HNN gain $K = 10$ was selected as a fixed value in this work. However, the optimal value of K depends on the operating conditions (load characteristics, noise level, transient frequency). An adaptive gain tuning scheme could adjust K in real time based on the estimation error or some other performance metric. Possible approaches include fuzzy logic based tuning, gradient descent on K itself, or reinforcement learning based tuning.

7.5.3 Extension to Three-Phase Systems

While the single-phase case is interesting for residential EV chargers, commercial and industrial charging stations are typically three-phase. The HNN and GI algorithms can be extended to three-phase systems using either the $\alpha\beta$ coordinates or by applying them independently to each phase. The three-phase HNN formulation and the three-phase DSOGI based GI formulation. These could be combined in a future study.

7.5.4 Weak Grid and Microgrid Scenarios

The present work assumes a stiff grid. In weak grid scenarios (where the source impedance is significant) and in microgrid scenarios (where the system may operate in islanded mode), the performance of the algorithms may change substantially. Future work could investigate:

- Performance of HNN and GI under weak grid conditions with varying source impedance.
- Seamless mode transition between grid-connected and islanded operation.
- Voltage and frequency control in islanded mode using the same SAPF hardware.
- Microgrid level energy management with multiple PV-Battery-EV nodes.

7.5.5 Improved Battery and EV Charger Modelling

Future work could use more sophisticated battery models, including electrochemical models, equivalent circuit models with multiple RC branches, and thermal models. The EV charger could be modelled with realistic CC-CV charging profiles and more complex front-end topologies (e.g. interleaved boost PFC, single-stage matrix-type chargers).

7.5.6 Stochastic Optimization for Sizing and Placement

The sizing of the PV array, battery capacity, SAPF rating and the placement of multiple charging stations across a distribution network are interesting optimization problems. These can be addressed using stochastic optimization techniques (e.g. genetic algorithm, particle swarm optimization) considering uncertainties in load profile, irradiance and EV arrival/departure patterns.

Appendix A

Simulation Parameters and Design Calculations

Appendix A: Design Parameters of Battery Interfaced PV Integrated Grid Connected System

The parameters listed below follow the configuration of Appendix III of Arora's thesis [104] for the battery interfaced PV integrated grid connected system, with the load and battery rating modified to suit the EV charging scenario considered in this work.

A.1 Grid and Source Parameters

Grid supply voltage V_s	110 V (rms), 1-phase, 50 Hz
Source side inductor L_s	1×10^{-6} H
Grid frequency f	50 Hz
Sampling time	50 μs

A.2 SAPF Parameters

Interfacing inductor L_f	3 mH
DC bus capacitance C_{dc}	3000 μF
Reference DC bus voltage V_{dc}^*	200 V
VSC topology	H-bridge (4 IGBTs with anti-parallel diodes)
IGBT switching frequency f_s	10 kHz
HCC hysteresis band h_{band}	±0.5 A

A.3 Nonlinear Load Parameters

Load topology	Single-phase 2-leg diode bridge rectifier with R-L load
R_{NL1} (heavy load condition)	20 Ω (corresponds to ≈ 6 A rms drawn)
R_{NL2} (light load condition)	120 Ω (corresponds to ≈ 1 A rms drawn)
L_{NL}	80 mH

A.4 PV Array Specifications (Kyocera Solar KD250GX-LFB2)

Maximum power P_{mp} per panel	250.022 W
Open-circuit voltage V_{oc}	36.9 V
Short-circuit current I_{sc}	9.09 A
Voltage at MPP V_{mp}	29.8 V
Current at MPP I_{mp}	8.39 A
Series connected modules per string	3
Cells per module	60
Parallel solar strings	1
Temperature coefficient of voltage	-0.32 %/°C
Temperature coefficient of current	+0.06 %/°C
Total array power (STC)	750 W

A.5 Boost Converter Parameters (for PV interface)

Boost inductor L_b	5 mH
Boost capacitor C_b	150 μF
Switching frequency	10 kHz
MPPT algorithm	Perturb & Observe (P&O)
MPPT step size δD	0.002
MPPT sampling interval	1 ms

A.6 Battery Specifications

Battery type	Lead-acid
Nominal voltage V_{batt}	154 V
Nominal capacity	20 Ah
Initial State of Charge (SOC)	90 %
Response time	0.1 s
SOC discharge cutoff	20 %
SOC charge cutoff	95 %

A.7 Bidirectional Buck-Boost Converter Parameters (for Battery interface)

Bidirectional inductor L_{bb}	2 mH
Bidirectional capacitor C_{bb}	470 μF
Switching frequency	5 kHz

A.8 Control Parameters

DC link PI controller K_p	0.1
DC link PI controller K_I	1.0
I_{loss} saturation limit	±5 A
HNN gain K	10
GI gain K	$\sqrt{2} \approx 1.414$
SOGI resonant frequency ω	314 rad/s (50 Hz)

A.9 Simulation Configuration

Software	MATLAB R2023a with Simscape Electrical
Solver	Fixed step (ode4 Runge-Kutta)
Time step	50 μs
Total simulation time	5 s
FFT window for THD	10 cycles (200 ms) in steady state

Appendix B: Key Design Calculations Summary

B.1 DC Link Voltage Calculation

$$V_{dc,min} = \sqrt{2}\, V_{rms} = \sqrt{2} \times 110 = 155.56 \text{ V}$$

Chosen value: $V_{dc} = 200$ V (28.6% margin)

B.2 DC Link Capacitance Calculation

$$C_{dc} = \frac{2K_1 V_{rms}\, a\, I\, t}{V_{dc}^2 - V_{dc1}^2}$$

With $K_1 = 0.5$, $V_{rms} = 110$ V, $I = 20$ A, $t = 0.02$ s, $V_{dc} = 200$ V, $V_{dc1} = 155.56$ V, $a = 1.2$:

$$C_{dc} = \frac{2 \times 0.5 \times 110 \times 1.2 \times 20 \times 0.02}{200^2 - 155.56^2} = 3341\ \mu\text{F}$$

Chosen value: $C_{dc} = 3000\ \mu$F

B.3 Interfacing Inductor Calculation

$$L_f = \frac{m\, V_{dc}}{4\, a\, f_s\, I_{crpp}}$$

With $m = 1$, $V_{dc} = 200$ V, $a = 1.2$, $f_s = 10$ kHz, $I_{crpp} = 1.5$ A:

$$L_f = \frac{1 \times 200}{4 \times 1.2 \times 10 \times 10^3 \times 1.5} = 2.77 \text{ mH}$$

Chosen value: $L_f = 3$ mH

Appendix C: Acronyms List

ADALINE	Adaptive Linear Neuron
ANF	Adaptive Notch Filter
APF	Active Power Filter
BES	Battery Energy Storage
BPF	Band Pass Filter
CC-CV	Constant Current - Constant Voltage
DC	Direct Current
DSO	Digital Storage Oscilloscope
DSOGI	Double Second Order Generalized Integrator
DSP	Digital Signal Processor
DSTATCOM	Distribution Static Compensator
DVR	Dynamic Voltage Restorer
EMI	Electromagnetic Interference
EV	Electric Vehicle
FFT	Fast Fourier Transform
FLANN	Functional Link Artificial Neural Network
FPGA	Field Programmable Gate Array
G2V	Grid to Vehicle
GI	Generalized Integrator
HCC	Hysteresis Current Controller
HNN	Hopfield Neural Network
IEEE	Institute of Electrical and Electronics Engineers
IGBT	Insulated Gate Bipolar Transistor
LFNN	Legendre Functional Neural Network
LLMF	Leaky Least Mean Fourth
LMS	Least Mean Square
LPF	Low Pass Filter
LVRT	Low Voltage Ride Through
MPC	Model Predictive Control
MPPT	Maximum Power Point Tracking
NN	Neural Network
P&O	Perturb and Observe
PCC	Point of Common Coupling
pf	Power Factor

Bibliography

[1] B. Singh, A. Chandra, and K. Al-Haddad, *Power Quality: Problems and Mitigation Techniques*. Chichester, U.K.: John Wiley & Sons, 2015.

[2] A. Moreno-Munoz, *Power Quality: Mitigation Technologies in a Distributed Environment*. London: Springer-Verlag, 2007.

[3] A. Ghosh and G. Ledwich, *Power Quality Enhancement Using Custom Power Devices*. New Delhi, India: Springer International Edition, 2009.

[4] H. J. Bollen, *Understanding Power Quality Problems*. New Delhi: Standard Publishers Distributors, 1st ed., 2001.

[5] C. Sankaran, *Power Quality*. New York: CRC Press, 2002.

[6] R. N. Beres, X. Wang, M. Liserre, F. Blaabjerg, and C. L. Bak, "A review of passive power filters for three-phase grid-connected voltage-source converters," *IEEE J. Emerg. Sel. Topics Power Electron.*, vol. 4, pp. 54–69, Mar. 2016.

[7] J. C. Das, "Passive filters – potentialities and limitations," *IEEE Trans. Ind. Appl.*, vol. 40, no. 1, pp. 232–241, 2004.

[8] E. F. El-Saadany, M. M. A. Salama, and A. Y. Chikhani, "Passive filter design for harmonic reactive power compensation in single-phase circuits supplying nonlinear loads," *IEE Proc. Gener. Transm. Distrib.*, vol. 147, pp. 373–380, 2000.

[9] H. Akagi, "Active harmonic filters," *Proc. IEEE*, vol. 93, pp. 2128–2141, Dec. 2005.

[10] J. Nastran, R. Cajhen, M. Seliger, and P. Jereb, "Active power filter for nonlinear AC loads," *IEEE Trans. Power Electron.*, vol. 9, pp. 92–96, Jan. 1994.

[11] R. A. Mastromauro, M. Liserre, and A. Dell'Aquila, "Control issues in single-stage photovoltaic systems: MPPT, current and voltage control," *IEEE Trans. Ind. Informat.*, vol. 8, pp. 241–254, May 2012.

[12] S. B. Kjaer, J. K. Pedersen, and F. Blaabjerg, "A review of single-phase grid-connected inverters for photovoltaic modules," *IEEE Trans. Ind. Appl.*, vol. 41, no. 5, pp. 1292–1306, 2005.

[13] M. Amir *et al.*, "Intelligent learning approach for transition control and protection of solar PV integrated electric vehicle charging station," *Sustainable Energy Technologies and Assessments*, vol. 64, p. 103712, Apr. 2024.

[14] S. Nayak and S. Mohanty, "Grid connected electric vehicle charging and discharging rate management with balance grid load," *Electrical Engineering*, vol. 105, pp. 595–572, Apr. 2023.

[15] "IEEE recommended practice and requirements for harmonic control in electric power systems." IEEE Std 519-2014 (Revision of IEEE Std 519-1992), 2014.

[16] A. Cavallini and G. C. Montanari, "Compensation strategies for shunt active-filter control," *IEEE Trans. Power Electron.*, vol. 9, pp. 587–593, Nov. 1994.

[17] J. Hafner, M. Aredes, and K. Heumann, "A shunt active power filter applied to high voltage distribution lines," *IEEE Trans. Power Del.*, vol. 12, pp. 266–272, Jan. 1997.

[18] T.-J. Park, G.-Y. Jeong, and B.-H. Kwon, "Shunt active filter for reactive power compensation," *Int. J. Electron.*, vol. 88, no. 12, pp. 1257–1269, 2001.

[19] H. Akagi, Y. Kanazawa, and A. Nabae, "Instantaneous reactive power compensators comprising switching devices without energy storage components," *IEEE Trans. Ind. Appl.*, vol. 20, no. 3, pp. 625–630, 1984.

[20] V. Khadkikar, A. Chandra, and B. N. Singh, "Generalized single-phase p-q theory for active power filtering: Simulation and DSP-based experimental investigation," *IET Power Electron.*, vol. 2, pp. 67–78, Jan. 2009.

[21] B. Singh and J. Solanki, "A comparison of control algorithms for DSTATCOM," *IEEE Trans. Ind. Electron.*, vol. 56, pp. 2738–2745, July 2009.

[22] M. Qasim, P. Kanjiya, and V. Khadkikar, "Artificial neural-network-based phase-locking scheme for active power filters," *IEEE Trans. Ind. Electron.*, vol. 61, pp. 3857–3866, Aug. 2014.

[23] P. Chittora, *Development of Functional Link Neural Network Based Control Algorithms for Power Quality Improvement Using Shunt Active Power Filter.* PhD thesis, Delhi Technological University, Delhi, India, 2018.

[24] P. Chittora, A. Singh, and M. Singh, "Chebyshev functional expansion based artificial neural network controller for shunt compensation," *IEEE Trans. Ind. Informat.*, vol. 14, pp. 3792–3800, Sept. 2018.

[25] P. Shah, I. Hussain, B. Singh, A. Chandra, and K. Al-Haddad, "GI-based control scheme for single-stage grid interfaced SECS for power quality improvement," *IEEE Trans. Ind. Appl.*, vol. 55, pp. 869–881, Jan. 2019.

[26] P. Shah, I. Hussain, and B. Singh, "A novel fourth-order generalized integrator based control scheme for multifunctional SECS in the distribution system," *IEEE Trans. Energy Convers.*, vol. 33, pp. 949–958, Sept. 2018.

[27] H. Saxena, A. Singh, and J. N. Rai, "Enhanced third-order generalized integrator-based grid synchronization technique for DC-offset rejection and precise frequency estimation," *Arab. J. Sci. Eng.*, vol. 46, pp. 9753–9762, 2021.

[28] M. H. J. Bollen, *Understanding Power Quality Problems: Voltage Sags and Interruptions.* New York: IEEE Press, John Wiley & Sons, 2000.

[29] "IEEE recommended practice for monitoring electric power quality." IEEE Std 1159-2009 (Revision of IEEE Std 1159-1995), 2009.

[30] B. Singh, P. Jayaprakash, D. P. Kothari, A. Chandra, and K. A. Haddad, "Comprehensive study of DSTATCOM configurations," *IEEE Trans. Ind. Informat.*, vol. 10, pp. 854–870, May 2014.

[31] IEEE Working Group on Power System Harmonics, “Power system harmonics: An overview,” *IEEE Trans. Power Apparatus and Systems*, vol. 102, no. 8, pp. 2455–2460, 1983.

[32] G. J. Wakileh, *Power Systems Harmonics.* New York: Springer, 2001.

[33] J. S. Subjak and J. S. McQuilkin, “Harmonics – causes, effects, measurements, and analysis: An update,” *IEEE Trans. Ind. Appl.*, vol. 26, no. 6, pp. 1034–1042, 1990.

[34] J. Schlabbach, D. Blume, and T. Stephanblome, *Voltage Quality in Electrical Power Systems.* Power Engineering and Energy Series, IEEE Press, 2001.

[35] M. Liserre, F. Blaabjerg, and S. Hansen, “Design and control of an LCL-filter based three-phase active rectifier,” in *Conf. Record 2001 IEEE Industry Applications Conf., 36th IAS Annual Meeting*, vol. 1, pp. 299–307, 2001.

[36] F. B. Libano *et al.*, “Simplified control of the series active power filter for voltage conditioning,” in *2006 IEEE Int. Symp. Ind. Electron.*, pp. 1706–1711, 2006.

[37] Z. Wang, Q. Wang, W. Yao, and J. Liu, “A series active power filter adopting hybrid control approach,” *IEEE Trans. Power Electron.*, vol. 16, no. 3, pp. 301–310, 2001.

[38] L. Moran, P. Werlinger, J. Dixon, and R. Wallace, “A series active power filter which compensates current harmonics and voltage unbalance simultaneously,” in *Proc. PESC ’95*, pp. 222–227, 1995.

[39] V. Khadkikar and A. Chandra, “UPQC-S: A novel concept of simultaneous voltage sag/swell and load reactive power compensations utilizing series inverter of UPQC,” *IEEE Trans. Power Electron.*, vol. 26, pp. 2414–2425, Sept. 2011.

[40] P. E. Melin *et al.*, “Analysis, design and control of a unified power-quality conditioner based on a current-source topology,” *IEEE Trans. Power Del.*, vol. 27, no. 4, pp. 1727–1736, 2012.

[41] S. Haykin, *Neural Networks and Learning Machines.* Upper Saddle River, NJ: Pearson Education, 2009.

[42] C. T. Lin and C. S. G. Lee, *Neural Fuzzy Systems: A Neuro-Fuzzy Synergism to Intelligent Systems.* Englewood Cliffs, NJ: Prentice-Hall.

[43] M. Cirrincione, M. Pucci, and G. Vitale, "A single-phase DG generation unit with shunt active power filter capability by adaptive neural filtering," *IEEE Trans. Ind. Electron.*, vol. 55, pp. 2093–2110, May 2008.

[44] M. Cirrincione, M. Pucci, G. Vitale, and A. Miraoui, "Current harmonic compensation by a single-phase shunt active power filter controlled by adaptive neural filtering," *IEEE Trans. Ind. Electron.*, vol. 56, pp. 3128–3143, Aug. 2009.

[45] H. Saxena, A. Singh, J. N. Rai, and M. Badoni, "PV integrated grid synchronization technique using modified SOGI-FLL and zero-crossing detector," *Electr. Eng.*, vol. 104, pp. 1361–1372, 2022.

[46] H. Saxena, A. Singh, and J. N. Rai, "Adaptive spline-based PLL for synchronisation and power quality improvement in distribution system," *IET Gener. Transm. Distrib.*, vol. 14, pp. 1311–1319, 2020.

[47] F. Xiao, L. Dong, L. Li, and X. Liao, "A frequency-fixed SOGI-based PLL for single-phase grid-connected converters," *IEEE Trans. Power Electron.*, vol. 32, pp. 1713–1719, Mar. 2017.

[48] A. Kulkarni and V. John, "Design of a fast response time single-phase PLL with DC offset rejection capability," in *2016 IEEE Applied Power Electronics Conf. (APEC)*, pp. 2200–2206, 2016.

[49] C. Zhang, X. Zhao, X. Wang, X. Chai, Z. Zhang, and X. Guo, "A grid synchronization PLL method based on mixed second- and third-order generalized integrator for DC offset elimination and frequency adaptability," *IEEE J. Emerg. Sel. Topics Power Electron.*, vol. 6, pp. 1517–1526, Sept. 2018.

[50] J. C. Patra, W. C. Chin, P. K. Meher, and G. Chakraborty, "Legendre-FLANN-based nonlinear channel equalization in wireless communication system," in *2008 IEEE Int. Conf. Systems, Man and Cybernetics*, pp. 1826–1831, 2008.

[51] H. H. Ali and M. T. Haweel, "Legendre neural networks with multi input multi output system equations," in *2012 7th Int. Conf. Computer Engineering & Systems (ICCES)*, pp. 92–97, 2012.

[52] S. S. Bayin, *Mathematical Methods in Science and Engineering*. Hoboken, NJ: Wiley, 2nd ed., 2006.

[53] R. Rasala, "The Rodrigues formulae and polynomial differential operators," *J. Math. Anal. Appl.*, vol. 84, no. 2, pp. 443–482, 1981.

[54] M. Scarpiniti, D. Comminiello, R. Parisi, and A. Uncini, "Nonlinear spline adaptive filtering," *Digital Signal Process.*, vol. 93, no. 4, pp. 772–783, 2016.

[55] M. Scarpiniti, D. Comminiello, G. Scarano, R. Parisi, and A. Uncini, "Steady-state performance of spline adaptive filters," *IEEE Trans. Signal Process.*, vol. 64, no. 4, pp. 816–828, 2016.

[56] C. de Boor, *A Practical Guide to Splines*, vol. 27 of *Applied Mathematical Sciences*. USA: Springer-Verlag, 2001.

[57] A. Candan, "An efficient filtering structure for Lagrange interpolation," *IEEE Signal Process. Lett.*, vol. 14, pp. 17–19, Jan. 2007.

[58] V. Valimaki, "A new filter implementation strategy for Lagrange interpolation," in *Proc. ISCAS'95*, vol. 1, pp. 361–364, 1995.

[59] A. Franck, "Efficient algorithms and structures for fractional delay filtering based on Lagrange interpolation," *J. Audio Eng. Soc.*, vol. 56, no. 12, pp. 1036–1056, 2008.

[60] G. L. Sicuranza and A. Carini, "On the BIBO stability condition of adaptive recursive FLANN filters with application to nonlinear active noise control," *IEEE Trans. Audio Speech Lang. Process.*, vol. 20, pp. 234–245, Jan. 2012.

[61] G. L. Sicuranza and A. Carini, “A generalized FLANN filter for nonlinear active noise control,” *IEEE Trans. Audio Speech Lang. Process.*, vol. 19, pp. 2412–2417, Nov. 2011.

[62] V. Kumar, K. M. M. Prabhu, and D. P. Das, “Block filtered-s least mean square algorithm for active control of non-linear noise systems,” *IET Signal Process.*, vol. 4, no. 2, pp. 68–180, 2010.

[63] G. L. Sicuranza and A. Carini, “On the accuracy of generalized hammerstein models for nonlinear active noise control,” pp. 1411–1416, 2006.

[64] N. Kumar, I. Hussain, B. Singh, and B. K. Panigrahi, “Implementation of multilayer fifth-order generalized integrator-based adaptive control for grid-tied solar PV energy conversion system,” *IEEE Trans. Ind. Informat.*, vol. 14, pp. 2857–2868, July 2018.

[65] N. Kumar, B. Singh, and B. K. Panigrahi, “PNKLMF-based neural network control and learning-based HC MPPT technique for multiobjective grid integrated solar PV based distributed generating system,” *IEEE Trans. Ind. Informat.*, vol. 15, pp. 3732–3742, June 2019.

[66] N. Kumar, I. Hussain, B. Singh, and B. K. Panigrahi, “Normal harmonic search algorithm-based MPPT for solar PV system and integrated with grid using reduced sensor approach and PNKLMS algorithm,” *IEEE Trans. Ind. Appl.*, vol. 54, pp. 6343–6352, Nov. 2018.

[67] N. Kumar, B. Singh, and B. K. Panigrahi, “ANOVA kernel Kalman filter for multi-objective grid integrated solar photovoltaic-distribution static compensator,” *IEEE Trans. Circuits Syst. I, Reg. Papers*, vol. 66, pp. 4256–4264, Nov. 2019.

[68] N. Kumar, B. Singh, B. K. Panigrahi, and L. Xu, “Leaky-least-logarithmic-absolute-difference-based control algorithm and learning-based InC MPPT technique for grid-integrated PV system,” *IEEE Trans. Ind. Electron.*, vol. 66, pp. 9003–9012, Nov. 2019.

[69] N. Kumar, B. Singh, and B. K. Panigrahi, “Framework of gradient descent least squares regression-based NN structure for power quality improvement in PV-integrated low-voltage weak grid system,” *IEEE Trans. Ind. Electron.*, vol. 66, pp. 9724–9733, Dec. 2019.

[70] T. Esram and P. L. Chapman, “Comparison of photovoltaic array maximum power point tracking techniques,” *IEEE Trans. Energy Convers.*, vol. 22, pp. 439–449, June 2007.

[71] B. Subudhi and R. Pradhan, “A comparative study on maximum power point tracking techniques for photovoltaic power systems,” *IEEE Trans. Sustain. Energy*, vol. 4, pp. 89–98, Jan. 2013.

[72] K. H. Hussein, I. Muta, T. Hoshino, and M. Osakada, “Maximum photovoltaic power tracking: An algorithm for rapidly changing atmospheric conditions,” *IEE Proc. Gener. Transm. Distrib.*, vol. 142, pp. 59–64, Jan. 1995.

[73] G. J. Kish, J. J. Lee, and P. W. Lehn, “Modelling and control of photovoltaic panels utilising the incremental conductance method for maximum power point tracking,” *IET Renew. Power Gener.*, vol. 6, pp. 259–266, July 2012.

[74] C.-S. Chiu and Y.-L. Ouyang, “Robust maximum power tracking control of uncertain photovoltaic systems: A unified T-S fuzzy model-based approach,” *IEEE Trans. Control Syst. Technol.*, vol. 19, pp. 1516–1526, Nov. 2011.

[75] E. Bianconi *et al.*, “A fast current-based MPPT technique employing sliding mode control,” *IEEE Trans. Ind. Electron.*, vol. 60, pp. 1168–1178, Mar. 2013.

[76] R. Khanaki, M. A. M. Radzi, and M. H. Marhaban, “Comparison of ANN and P&O MPPT methods for PV applications under changing solar irradiation,” in *2013 IEEE Conf. Clean Energy and Technology (CEAT)*, pp. 287–292, 2013.

[77] M. Karimi, H. Mokhlis, K. Naidu, S. Uddin, and A. H. A. Bakar, “Photovoltaic penetration issues and impacts in distribution network – a review,” *Renew. Sustain. Energy Rev.*, vol. 53, pp. 594–605, Jan. 2016.

[78] H. Liu, P. C. Loh, X. Wang, Y. Yang, W. Wang, and D. Xu, “Droop control with improved disturbance adaption for a PV system with two power conversion stages,” *IEEE Trans. Ind. Electron.*, vol. 63, pp. 6073–6085, Oct. 2016.

[79] C. Jain and B. Singh, “An adjustable DC link voltage-based control of multifunctional grid interfaced solar PV system,” *IEEE J. Emerg. Sel. Topics Power Electron.*, vol. 5, pp. 651–660, June 2017.

[80] M. Mirhosseini, J. Pou, and V. G. Agelidis, “Single- and two-stage inverter-based grid-connected photovoltaic power plants with ride-through capability under grid faults,” *IEEE Trans. Sustain. Energy*, vol. 6, pp. 1150–1159, July 2015.

[81] B. Singh, C. Jain, and S. Goel, “ILST control algorithm of single-stage dual purpose grid connected solar PV system,” *IEEE Trans. Power Electron.*, vol. 29, pp. 5347–5357, Oct. 2014.

[82] V. Jain, I. Hussain, and B. Singh, “A HTF-based higher-order adaptive control of single-stage grid-interfaced PV system,” *IEEE Trans. Ind. Appl.*, vol. 55, pp. 1873–1881, Mar. 2019.

[83] Y. Singh, I. Hussain, S. Mishra, and B. Singh, “Adaptive neuron detection-based control of single-phase SPV grid integrated system with active filtering,” *IET Power Electron.*, vol. 10, pp. 657–666, 2017.

[84] P. Shukla and B. Singh, “Recursive digital filter based control for power quality improvement of grid tied solar PV system,” *IEEE Trans. Ind. Appl.*, vol. 56, pp. 3412–3421, July 2020.

[85] N. M. C. M., Y. Singh, S. B. Q. Naqvi, B. Singh, and J. Pychadathil, “Multi-objective solar power conversion system with MGI control for grid integration at adverse operating conditions,” *IEEE Trans. Sustain. Energy*, vol. 11, pp. 2901–2910, Oct. 2020.

[86] V. Rallabandi, O. M. Akeyo, N. Jewell, and D. M. Ionel, “Incorporating battery energy storage systems into multi-MW grid connected PV systems,” *IEEE Trans. Ind. Appl.*, vol. 55, pp. 638–647, Jan. 2019.

[87] V. Karthikeyan and R. Gupta, “Varying phase angle control in isolated bidirectional DC-DC converter for integrating battery storage and solar PV system in standalone mode,” *IET Power Electron.*, vol. 10, pp. 471–479, 2017.

[88] “Electric vehicle conductive charging system.” IEC 61851-1.

[89] V. Kaura and V. Blasko, “Operation of a phase locked loop system under distorted utility conditions,” *IEEE Trans. Ind. Appl.*, vol. 33, pp. 58–63, Jan. 1997.

[90] M. Karimi-Ghartemani and M. R. Iravani, “A method for synchronization of power electronic converters in polluted and variable-frequency environments,” *IEEE Trans. Power Syst.*, vol. 19, pp. 1263–1270, Aug. 2004.

[91] C. Subramanian and R. Kanagaraj, “Single-phase grid voltage attributes tracking for the control of grid power converters,” *IEEE J. Emerg. Sel. Topics Power Electron.*, vol. 2, pp. 1041–1048, Dec. 2014.

[92] J. Svensson, “Synchronization methods for grid-connected voltage source converters,” *Proc. IEE Gener. Transm. Distrib.*, vol. 148, pp. 229–235, May 2001.

[93] A. B. Shitole, H. M. Suryawanshi, S. Sathyan, and M. M. Renge, “Adaptive notch filter based synchronization technique for integration of distributed generation systems to utility grid,” in *IECON 2014 - 40th Annual Conf. IEEE Ind. Electron. Society*, pp. 5457–5461, 2014.

[94] S. Golestan, M. Ramezani, J. M. Guerrero, F. D. Freijedo, and M. Monfared, “Moving average filter based phase-locked loops: Performance analysis and design guidelines,” *IEEE Trans. Power Electron.*, vol. 29, pp. 2750–2763, June 2014.

[95] Y. F. Wang and Y. W. Li, “Three-phase cascaded delayed signal cancellation PLL for fast selective harmonic detection,” *IEEE Trans. Ind. Electron.*, vol. 60, pp. 1452–1463, Apr. 2013.

[96] B. P. McGrath, D. G. Holmes, and J. J. H. Galloway, "Power converter line synchronization using a discrete fourier transform (DFT) based on a variable sample rate," *IEEE Trans. Power Electron.*, vol. 20, pp. 877–884, July 2005.

[97] S. Swain and B. Subudhi, "Grid synchronization of a PV system with power quality disturbances using unscented Kalman filtering," *IEEE Trans. Sustain. Energy*, vol. 10, pp. 1240–1247, July 2019.

[98] M. A. Khanesar, E. Kayacan, M. Teshnehlab, and O. Kaynak, "Extended Kalman filter based learning algorithm for type-2 fuzzy logic systems and its experimental evaluation," *IEEE Trans. Ind. Electron.*, vol. 59, pp. 4443–4455, Nov. 2012.

[99] P. Shah and B. Singh, "Kalman filtering technique for rooftop-PV system under abnormal grid conditions," *IEEE Trans. Sustain. Energy*, vol. 11, pp. 282–293, Jan. 2020.

[100] J.-H. Kim, S.-W. Lee, S.-R. Lee, T.-W. Lee, and C.-Y. Won, "Power quality control using the Goertzel algorithm for grid-connected system," in *INTELEC 2009 - 31st Int. Telecommunications Energy Conf.*, pp. 1–3, 2009.

[101] Y. Singh, I. Hussain, B. Singh, and S. Mishra, "Single-phase solar grid-interfaced system with active filtering using adaptive linear combiner filter-based control scheme," *IET Gener. Transm. Distrib.*, vol. 11, no. 8, pp. 1976–1984, 2017.

[102] T.-F. Wu, H.-S. Nien, C.-L. Shen, and T.-M. Chen, "A single-phase inverter system for PV power injection and active power filtering with nonlinear inductor consideration," *IEEE Trans. Ind. Appl.*, vol. 41, pp. 1075–1083, July 2005.

[103] P. Chaudhary and M. Rizwan, "QNBP NN-based i cos ϕ algorithm for PV systems integrated with LV/MV grid," *Soft Computing*, vol. 25, no. 4, p. 2599, 2021.

[104] A. Arora, *Design and Development of Adaptive Control Algorithms for Shunt Active Power Filter in PV Integrated Grid Connected Systems.* PhD thesis, Delhi Technological University, Delhi, India, 2023.

HNN method based PV integrated grid connected EV charging system.pdf

Birla Institute of Technology, Mesra

Document Details

Submission ID

trn:oid:::3117:595251133

Submission Date

May 28, 2026, 6:57 PM GMT+5:30

Download Date

May 28, 2026, 7:10 PM GMT+5:30

File Name

HNN method based PV integrated grid connected EV charging system.pdf

File Size

865.5 KB

100 Pages

22,351 Words

117,157 Characters

17% Overall Similarity

The combined total of all matches, including overlapping sources, for each database.

Filtered from the Report

- Bibliography
- Small Matches (less than 8 words)

Exclusions

- 10 Excluded Matches

Match Groups

313 Not Cited or Quoted 16%
Matches with neither in-text citation nor quotation marks

19 Missing Quotations 1%
Matches that are still very similar to source material

1 Missing Citation 0%
Matches that have quotation marks, but no in-text citation

0 Cited and Quoted 0%
Matches with in-text citation present, but no quotation marks

Top Sources

13%	🌐	Internet sources
13%	📖	Publications
0%	👤	Submitted works (Student Papers)

Integrity Flags

1 Integrity Flag for Review

Replaced Characters
178 suspect characters on 22 pages
Letters are swapped with similar characters from another alphabet.

Our system's algorithms look deeply at a document for any inconsistencies that would set it apart from a normal submission. If we notice something strange, we flag it for you to review.

A Flag is not necessarily an indicator of a problem. However, we'd recommend you focus your attention there for further review.

Match Groups

313 Not Cited or Quoted 16%
Matches with neither in-text citation nor quotation marks

19 Missing Quotations 1%
Matches that are still very similar to source material

1 Missing Citation 0%
Matches that have quotation marks, but no in-text citation

0 Cited and Quoted 0%
Matches with in-text citation present, but no quotation marks

Top Sources

13%	Internet sources
13%	Publications
0%	Submitted works (Student Papers)

Top Sources

The sources with the highest number of matches within the submission. Overlapping sources will not be displayed.

1	Internet	**dspace.dtu.ac.in:8080**	**1%**
2	Internet	**vdoc.pub**	**<1%**
3	Publication	**Ankita Arora, Alka Singh. "Design and analysis of functional link artificial neural n...**	**<1%**
4	Internet	**documents.mx**	**<1%**
5	Publication	**Lecture Notes in Electrical Engineering, 2015.**	**<1%**
6	Internet	**ir.library.nitw.ac.in:8080**	**<1%**
7	Internet	**cupdf.com**	**<1%**
8	Internet	**dokumen.pub**	**<1%**
9	Internet	**unsworks.unsw.edu.au**	**<1%**
10	Internet	**core.ac.uk**	**<1%**

HNN method based PV integrated grid connected EV charging system.pdf

Birla Institute of Technology, Mesra

Document Details

Submission ID	trn:oid:::3117:595251133
Submission Date	May 28, 2026, 6:57 PM GMT+5:30
Download Date	May 28, 2026, 7:14 PM GMT+5:30
File Name	HNN method based PV integrated grid connected EV charging system.pdf
File Size	865.5 KB

100 Pages

22,351 Words

117,157 Characters

*% detected as AI

AI detection includes the possibility of false positives. Although some text in this submission is likely AI generated, scores below the 20% threshold are not surfaced because they have a higher likelihood of false positives.

Caution: Review required.

It is essential to understand the limitations of AI detection before making decisions about a student's work. We encourage you to learn more about Turnitin's AI detection capabilities before using the tool.